Chapter 2

Detector for the Linear Collider

General Detector Concepts and Detector Performance

Conveners: M. Martinez, D.J. Miller, M. Piccolo

Working Group: A. Andreazza, M. Battaglia, G. Blair, G. Daskalakis, A. Juste, A. Kyriakis, C. Markou, H.U. Martyn, H. Nowak, I. Riu, M. Sachwitz, H.J. Schreiber, D. Schulte, R. Settles, R. Shanidze, C. Shepherd-Themistocleous, S. Shichanin, E. Simopoulou, R. Vuopionperä, C. Troncon

Detector Subsystems

Conveners: M. Mazzucato, D. Saxon, R. Settles

Working Group: S. Aïd, A. Andreazza, P. Bambade, T. Barklow, W. Bartel, M. Battaglia, R. Bellanzzini, S. Bertolucci, G. Blair, R. Brinkmann, I. Brock, R. Brown, J. Bürger, P.J. Bussey, M. Caccia, P. Checchia, G. Coignet, P. Colas, P. Clarke, C. Damerell, M. David, A. De Roeck, E. Elsen, E. Fernandez, Y. Giomataris, T. Greenshaw, R. Heuer, C. Heusch, N. Holtkamp, P. Hüntemeyer, P. Janot, L. Jönsson, F.P. Juster, B.J. King, F. Kircher, V. Korbel, U. Kötz, Y. Kurihara, P. Le Du, M. Leenen, W. Lohmann, C. Luci, L. Mandelli, M. Martinez, C. Meroni, J. Meyer, D. Miller, R. Nahnhauer, O. Napoly, R. Nania, R. Orava, M. Piccolo, M. Pohl, D. Reed, F. Richard, A. Rousarie, H.-G. Sander, U. Schneekloth, H.J. Schreiber, S. Schreiber, D. Schulte, C. Shepherd-Themistocleous, F. Simonetto, K. Sinram, A. Skillman, A. Sopczak, P. Steffen, H. Steiner, J. Steuerer, G. Tonelli, M. Tonutti, C. Troncon, C. VanderVelde, G. Vegni, A. Wagner, N. Walker, M. Weber, W. Wiedenmann, G.W. Wilson, K. Zapfe-Düren

Collider-Experiment Interface

Conveners: N. Holtkamp, M. Leenen, O. Napoly

Working Group: G. Bardin, R. Brinkmann, C. Cavata, S. Drozhdin, J.-P. Jorda, N. Mokhov, M. Sachwitz, H.J. Schreiber, S. Schreiber, D. Schulte, R. Settles, K. Sinram, N. Walker, K. Zapfe-Düren

Contents

2.2 Subdetectors

2.2.1 Silicon Vertex Detector and Forward Tracker

Silicon detectors have become essential tools at fixed target and collider experiments [1, 2, 3]. The extreme accuracy of microstrip detectors [4, 5, 6] and the unique pattern recognition capability of pixel detectors [7, 8] can guarantee the full exploitation of the LC physics program for which excellent tracking and vertexing for heavy quark jet tagging are required. The silicon tracking has been designed to guarantee high quality tracking down to 100 mrad. It is divided into a vertex detector and a forward tracker.

The impact parameter resolution is the key figure of merit of the vertex detector performance. An $r\phi$ impact parameter resolution of better than $10\,\mu\mathrm{m} \oplus \frac{30\,\mu\mathrm{m\,GeV}/c}{p\ \sin^{3/2}\theta}$ has been assumed in Tab. 2.1.2 to give e.g. efficient Higgs selection. In the rz projection a similar resolution is required.

The forward tracking is important in e.g. $\mathrm{W^+W^-}$ physics for the charge identification of leptons from W decays in order to measure the W couplings. The absolute c.m.s. energy determination [9] also stresses good track measurement in the forward direction. The same is true for the measurement of the acollinearity of Bhabha events in order to determine the luminosity spectrum [10]. The benchmark for the forward tracking is therefore a momentum resolution of $\sigma_p/p < 20\,\%$ for particles in the energy range of 100 to 250 GeV and a polar angle resolution of $\sigma_\theta < 200\,\mu$rad down to the lowest possible polar angle.

2.2.1.1 Detector Layout

Vertex Detector. The impact parameter resolution is determined by both the single point precision and the detector layout. The detector technology and the radius of the innermost detector layer are constrained by the expected occupancies. These are due to both the track density in jets and the accelerator induced background. For the backgrounds, the current final focusing scheme and the 3 T magnetic field safely set the beam pipe radius at 2 cm and the first measurement plane at 2.5 cm. The track overlap in physics events at this radius is shown in Fig. 2.2.1 for the example reaction of $\mathrm{t\bar{t}}$ final states at $\sqrt{s} = 500$ GeV. The distributions show that a low level of ambiguity cannot be achieved with strip detectors. The situation is considerably better for pixel devices which are thus clearly preferred. The same conclusion can be drawn from the background hit density at $r = 2.5$ cm, where $\sim 10^{-2}$ hits/mm^2 are expected for each bunch crossing in TESLA and ~ 1 hit/mm^2 for each train crossing in SBLC (see Section 2.4).

Once the innermost layer radius is fixed, the interplay between the single point resolution and the lever arm to the outermost vertex detector layer determines the final impact parameter resolution; a detailed Kalman-filter based track fit, taking into

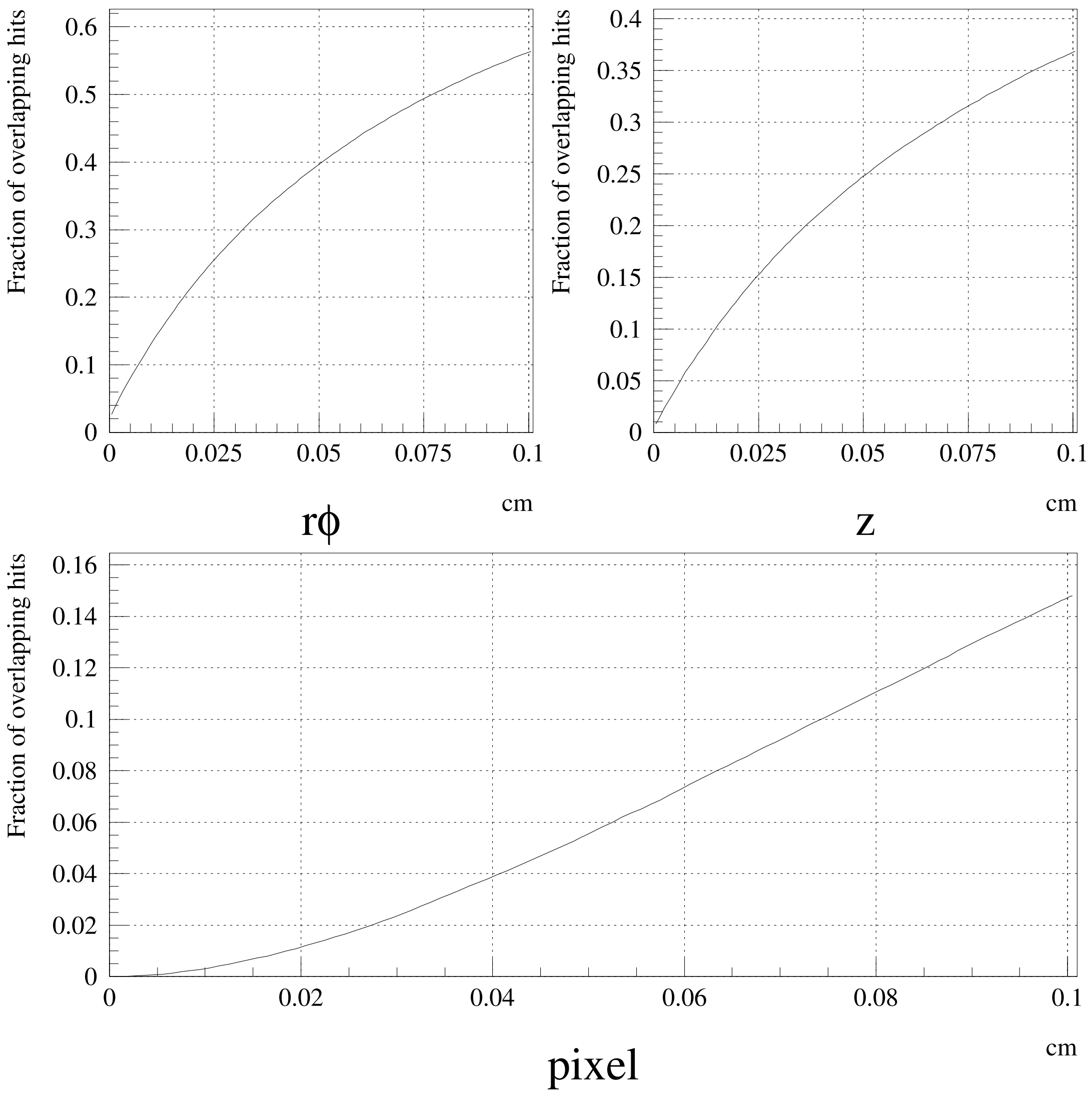

Figure 2.2.1: *Fraction of overlapping hits for the inner layer at* 2.5 cm *radius, as a function of the two-track resolution for $r\phi$ strips and z strips (upper plots) and for pixels (lower plot). The generated events were* $\mathrm{t\bar{t}}$ *final states at* $\sqrt{s} = 500\,\mathrm{GeV}$. *For the upper plots, the $r\phi$ strips are* 10 cm *long in z, and the z strips are* 2 cm *long in $r\phi$.*

account the full set of tracking chambers as specified in the subsequent sections, shows the design performance can be achieved with a single point resolution of 10 μm and a vertex detector outer layer at 10 cm radius from the interaction point.

Intermediate layers are needed to optimize the pattern recognition, and their number depends on the final detector technology:

- For Active Pixel Sensors (APS), the simplest possible geometry consists of one additional intermediate layer at 6 cm radius. A detailed simulation has shown that ambiguities at a few percent level can be obtained with a pattern recognition algorithm which starts by extrapolating a track element from the main tracker to the outermost vertex detector layer. The innermost layer extends down to 15° in polar angle, providing a precise measurement near the interaction point, in the angular region where b-tagging is effective. The mid and outer barrel layers will cover the 30° to 150° range. Each of these two layers will be complemented by an endcap, inclined by 30° with respect to the beam line and extending to the mask limit. The barrel acceptance and the cone inclination have been chosen in order to guarantee $\sigma_z \approx 10\,\mu$m also for inclined tracks. At the same time, the endcap geometry reduces the multiple scattering.

- For Charge Coupled Devices (CCD), a five layer design would allow stand-alone pattern recognition which would be desirable because of the longer readout time and the higher integrated background. A design for a CCD-based vertex detector at an X-band linear collider has recently been completed [11].

Irrespective of the detector technology, an azimuthal modularity of ~30-40° preserves the optimal $r\phi$ resolution and is also feasible for the innermost layer. Overlap between neighboring modules is foreseen for detector alignment using particle tracks.

The vertex detector has a total length of $\sim$ 60 cm, about the same size as the LEP vertex detectors, and is mounted on the inside of the intermediate tracker (see Figs. 2.1.2 and 2.2.3). Different options for the mechanics and cooling may be conceived, depending on the detector technology. For APSs, either ladders housing cooling pipes or a homogeneous support structure acting also as a heat pipe can be imagined. For CCDs, cooling to 180 K has to be foreseen. The repeater electronics might be housed in conical cards outside the detector region. According to the present experience at LEP/SLC/HERA, survey, internal and relative alignment of the vertex detector is feasible.

Forward Tracker. The forward tracker consists of two internal disks of pixel detectors and three external disks of microstrip detectors (see Fig. 2.1.2). In the forward region the emphasis is on high momentum isolated particle tracking. It is important to have the longest possible lever arm to improve both the momentum and angular resolution.

The internal pixel detector disks complement the precision measurement of the vertex detector endcaps, providing two additional space points. These planes are located before the beginning of the mask, at $z = \pm 40$ cm and ± 50 cm, with 12 cm outer radius. The inner radius should be $\geq$ 4 cm to avoid entering into the envelope of particles produced by beamstrahlung.

For the external part of the forward tracker, silicon microstrips are used. In this region, projective devices can stand the track density and possible ambiguities are solved using the pixel points in the inner part of the tracker. Microstrips provide easily an extremely good point resolution with a fairly low number of channels. Furthermore, a track trigger in the angular region not covered by the inner tracker can be foreseen. Detectors are arranged in three layers, at $z = \pm$ 120, 140 and 160 cm, with an inner sensitive radius corresponding to a coverage down to the mask at about $\theta = 5°(7°)$ for TESLA (SBLC) and with an outer radius of 30 cm.

2.2.1.2 Detector Technologies for the Vertex Detector

The development of high resolution pixel detectors is currently evolving in two main directions: Active Pixel Sensors [12] and Charge Coupled Devices [13]). Both types of detectors have been successfully used in experimental apparatus [14, 15, 16] and an intense R&D program is taking place for more demanding future applications [17, 18, 19]. Both detector technologies have appealing characteristics for the linear collider environment. In the following, the main characteristics of the two options are briefly compared.

Detector thickness. In order to achieve a good signal-to-noise ratio, S/N, silicon microstrips and APS detectors have been fabricated up to now with typically 300 μm thickness. For hybrid APSs, the bump-bonded VLSI chip has also to be accounted for and adds about 300 μm to the detector. Thus the total thickness would be about 0.6 % of a radiation length, which would increase to $> 1\,\%X_0$ per layer once the mechanical support is included. The current results on low noise integrated pre-amplifiers [20] and the tiny single cell capacitance allow the possibility of reducing the detector thickness to 150 μm with a $S/N \approx 25$ [8, 21]. Back-thinning of the VSLI chip after bump bonding has been proven down to 50 μm thickness [22], so that the overall thickness would then be about $0.8\,\%X_0$ including the now dominant mechanical support.

Charge Coupled Devices built for the SLD vertex detector [14] are 150 μm thick. They are glued to a 380 μm-thick beryllium oxide mother card and support structure, giving an overall thickness of $0.36\,\%X_0$ per layer. In future, the CCDs can be thinned down to approximately 20 μm, using a procedure now being pioneered for astronomical applications. Also the mother board layout can be simplified, so that the single layer thickness can be reduced to about $0.12\,\%X_0$.

At the moment a 1 mm thick beryllium beam pipe is assumed, so that the multiple scattering term in the impact parameter design performance requires the detector thickness in the innermost layer to be $1\,\%X_0$ or less. Moreover, in order to minimize the amount of material in front of the calorimeters and to optimize the matching with the main tracker, an overall thickness of $< 3\,\%X_0$ is envisaged. Both constraints are well within the specifications of the detectors considered, either with the APS three layer geometry or the CCD five layer geometry, including the cryostat wall ($0.5\,\%X_0$) in the latter case.

Pixel size. The pixel size, the S/N and the track incidence angle determine the single point resolution. The current CCDs developed for the SLD vertex detector have a $20\times20\,\mu\mathrm{m}^2$ pixel size and provide $\sim 5\,\mu$m spatial resolution. Because of the $20\,\mu$m thick sensitive region, the resolution is not degraded for inclined tracks. For the APS solution, the pixel size is determined by the bump bonding technique and the integration scale of the readout electronics. Presently a $100 \times 100\,\mu\mathrm{m}^2$ pixel size is feasible [17]. In $r\phi$ the resolution of an effective $50\,\mu$m pitch is achieved either by utilizing $E \times B$ to induce the sharing of charge carriers between staggered adjacent rows [17] and/or by designing interleaved pixels to give analogue capacitive charge division to the nearest neighboring readout pixels [23], as in microstrip detectors [24, 25]. Assuming $S/N \approx 25$, the resolution for orthogonal tracks is $10\,\mu$m [6]. The rz resolution is affected by the incident angle, and a graded pitch similar to the DELPHI solution [26] could be used. Increasing the pixel pitch in z as $\frac{\mathrm{thickness}}{\tan(\theta)}$, the track always crosses the detector at the optimal angle, and the resolution is $\sigma_z \approx \frac{\mathrm{pitch}}{(S/N)}$ [6]. Thus the design point resolution can be obtained down to polar angles of 30°.

Readout scheme. The use of APSs at the linear collider experiment will benefit from the characteristics of the VLSI front end electronics being developed for LHC pixel detectors [17, 18]. In particular, the possibility of fast gating and time stamping the pixel hits within 25 ns would allow a considerable reduction of background hits. It would limit the background accumulation to a single bunch in TESLA; in the SBLC with 6 ns bunch spacing the background would be integrated over four bunches. Using the LHC front-end pixel electronics a simultaneous sparse data scan would allow skipping over empty pixels at a $\sim$ 1 GHz rate, while addressing fired pixels at $\sim$ 100 ns/pixel.

The CCD readout time is intrinsically limited by the charge transfer clock. Currently at SLD the readout time is $\approx$ 150 ms with a 10 MHz readout clock. For the future 50 MHz may be envisaged, so that the detector could read out between two linac cycles but with background accumulated throughout the train. The higher background from the TESLA train could be substantially reduced by a combination of fast-clearing the detector at intervals of 50 pulses ($35\,\mu$s) and pushing the beams out of collision with a kicker after a good trigger. However it may be necessary to permit a high trigger rate in order to measure novel processes with very small energy deposition in the detector (e.g. $\tilde{\chi}^+ \to \tilde{\chi}^0 + \cdots$ with small chargino/neutralino mass difference). Then it will be necessary to permit background accumulation throughout the whole train, corresponding for TESLA to $\sim 7\,\mathrm{hits/mm^2}$. In this case about 0.3 % of the innermost layer would be occupied by background hits.

Note that the CCD readout is inherently dead-time free. There is no problem in reading out any number of triggers in the train. Whether the fast clear option is implemented or not, the CCD option makes no stringent demands on the inter-bunch spacing (708 ns for TESLA down to 4 ns for the SBLC).

Radiation damage. SBLC and X-band machines can be considered friendly as far as radiation is concerned. In the case of TESLA the zero degree crossing angle has the advantage of minimizing the dead cone of the detector, but it also means that the swathe of beamstrahlung photons is dumped fairly close to the detector. A potential source of radiation damage is created due to photo disintegration neutrons which are reflected back into the detector from the dump.

Neutrons are much more damaging than electromagnetic radiation. CCDs of the type currently available for charged particle detection would be limited to $\sim 3 \cdot 10^9\,\mathrm{n/cm^2}$. Neutrons from the dump would be catastrophic ($\sim 4 \cdot 10^{11}\,\mathrm{n/cm^2 \cdot year}$), were it not for the mask in the aperture of the final quadrupoles, which reduces the flux by a factor of $\sim 10^3$. This translates to a detector lifetime in the TESLA environment of at least four years. Furthermore, there is rapid progress in hardening CCDs with respect to neutron damage (a factor 10 is likely to result from supplementary channel developments and maybe more from switching to p channel devices).

Another source is neutrons generated from the beamstrahlung background absorbed within the detector. Preliminary indications [27] are that this flux could amount to around $3{\cdot}10^9$ neutrons/cm^2·year and lead to an inadequate CCD lifetime (without the previously mentioned hardening factors). This flux estimate however depends critically on the absorbing material within the detector volume, and for example lining the mask surfaces with polyboron could give a major reduction. Detailed simulations are necessary in this area, following the prescription by the LHC collaborations.

The APSs and front end electronics for LHC are expected to stand up to 10^{15} n/cm^2 even if type inversion occurs [17, 18], so they are well suited for the linear collider environment.

Finally, the dose by the charged particle flux amounts to $\sim 10\,\mathrm{krad}$ per year (10^7 s) and is completely negligible.

2.2.1.3 Forward Tracker Technology

As mentioned earlier, backgrounds make pixels for the inner discs and strips for the outer discs the appropriate choices. The amount of material must be kept at a minimum for the measurement of Bhabha electron tracks in this angular region.

Forward tracker pixels. The discs at $z = 40$ and 50 cm (shown in Fig. 2.1.2) will use pixels. Due to the higher background and particle flux in the forward region, APS detectors are more suitable than CCD devices. APS detectors in the forward region can use a mechanical structure similar to that proposed for the vertex detector. The detectors could be mounted on a ceramic substrate which also serves as a heat pipe for the cooling components near the beam pipe.

Arrangement of the detector modules in disks perpendicular to the beam axis provides good mechanical stability. A 30° modularity as in the barrel can be achieved with trapezoidal detectors cut from standard 5″ wafers. With this geometry, forward APSs can exploit neither the track crossing angle nor the $E \times B$ effect to improve the resolution via charge sharing among different pixels. However a pixel size of $50\,\mu$m in ϕ and $200\,\mu$m in r and binary readout provide adequate resolution and two-particle separation.

Forward tracker microstrips. The outer disks at $z = 120$, 140 and 160 cm could be made of double-sided microstrip detectors or of single-sided detectors glued back to back with perpendicular orientation of the strips to provide space points in each layer. The latter solution is cheaper than double-sided detectors but contains more material, so that the choice can be made only after assessing the effect on the measurement of the Bhabha electrons. Each disk is composed of 24 detector modules, each consisting of two daisy chained microstrip detectors. The modules are supported on the inner wall of the TPC. The 20 cm spacing between the detector planes is chosen to allow the insertion of the repeater electronics cards on additional wheels interleaved with the detector wheels. Careful design work is needed to keep the amount of material low for the Bhabha measurement.

The lower angle acceptance of the detector is determined by the mask and the space needed for beam-spot monitor hardware and other services (see Section 2.4). In the TESLA design the outside mask angle is about 80 mrad, so that the forward tracker can cover the polar angles down to 5° with small gaps at appropriate positions between detectors for the services. For the SBLC the outer mask angle is about 120 mrad, and the forward trackers would cover down to 7°.

A single point resolution below $25\,\mu$m [6] can be achieved for a $S/N \approx 20$ with a $100\,\mu$m strip pitch detector, reading out every second strip to take advantage of capacitive charge division. It has been shown that silicon detectors have a time resolution sufficient to identify the bunch crossing [28, 29], and a fast readout time can be achieved by sparse data scan [30] or by integrated pipelines [31].

An interesting feature is the possibility of having a track trigger in the forward region. A first level trigger based on silicon detectors has already been realized for the HERA detectors [32, 33]. The use of microstrip detectors for trigger purposes requires the development of dedicated VLSI electronics [34, 35], and the goal looks within the reach of currently evolving microelectronics technologies.

2.2.1.4 Discussion of the Vertex Detector Options

In order to compare the CCD and APS options, the SLD algorithm ZVTOP for topological vertexing [36], which optimally disentangles the tracks associated with the primary, secondary and tertiary vertices (if any) in the jet, was used. The analysis then determines the invariant mass of the reconstructed heavy hadron decay, together with the transverse momentum, p_t, of the decay tracks with respect to the heavy hadron flight path. These kinematic quantities are combined, making allowance for missing neutral decay products, to determine the 'p_t-added mass' M_{p_t}. The vertex topology in the jet, together with the magnitude of M_{p_t}, is used to classify the jet as light-quark, c-quark or b-quark. The major challenge to achieve reasonable b/c discrimination.

It should be emphasized that this procedure is not yet completely optimized, but it already provides a valid benchmark for comparing various detector options. Further details on the present study may be found in the complete report [37].

An equal mixture of b and c jets of energy 50 GeV is generated using JETSET 7.4 with the Peterson fragmentation function, within the polar angle range $|\cos\theta| \leq 0.7$, so that the tracks from the jet are well-contained within the vertex detector aperture. The performances of the CCD and APS vertex detector options are simulated by appropriately smearing the charged particle tracks in both the $r\phi$ and rz projections, according to their momenta and directions. The smeared tracks are then processed by ZVTOP to determine the jet flavor. Knowing the generated 4-vectors for the jet permits the efficiency and purity of the flavor assignment to be determined, as a function of the cut variable M_{p_t}. Additional cuts are used for the c tag; for details see Ref. [36].

This procedure has been repeated for jet energies 100 and 200 GeV, and is found to give very similar results over this range. The results for b identification with 50 GeV jet energy are shown in Fig. 2.2.2(a) and for c identification in Fig. 2.2.2(b). It is clear that significant gains can be made by reducing the beam pipe radius, pixel size and material thickness. This may require a smaller beam pipe than in the present TESLA and SBLC designs, with consequent changes to the final-focus optics and collimation in the machine. Beauty signals are not quite so difficult to resolve, but will also be improved by having the best possible resolution.

2.2.2 Intermediate Tracker

The intermediate tracker serves to link tracks between the vertex detector and the main tracker, to detect secondary vertices for longer-lived particles, and to give a fast trigger on charged particles. As pointed out in Tab. 2.1.1, the amount of material should be minimized in the whole tracking volume because of the backgrounds from beam-beam effects; about 600 (150) photons of 1 MeV energy traverse the volume for each TESLA (SBLC) bunch crossing. Also the end flanges should be as thin as possible for the measurement of Bhabhas in the forward tracker (see Section 2.2.1.3). The multi-cellular drift chamber "Wellblechkammer", or Honeycomb chamber, made of thin-walled plastic cells in a self-supporting structure with no need for heavy flanges or massive walls, fulfills these two conditions nicely. A cross section through the intermediate detector is seen in Fig. 2.2.3.

The other technique studied for the intermediate tracker was scintillating fibers enclosing a TEC-type drift chamber as in L3 and is described in detail in Ref. [38].

Honeycomb Chamber

Prototype detectors with hexagonal shaped cells made of conductive plastic have been made and tested [39]. The cell size was 15 mm for the hexagons, and the cells were formed from foils of Makrofol KL3-1009, which is conducting and has good mechanical properties. The cell geometry was formed by pressing the foil at 180-210°C into a die consisting of groves with the desired cell pitch and having half of the hexagonal shape. Two foils were glued together to form a primary layer of cells, and these primary layers were then glued to form a block. This block can be shaped in a multiangle cylindrical form as shown in Fig. 2.2.3. Chambers of similar design are presently being manufactured for the Hera-B experiment.

This device will also be the support for the vertex detector and the four inner discs of the forward tracker. The radial thickness of the Honeycomb chamber can be kept to between 0.2 and 0.5 % X_0, depending on the number of cells chosen radially. The end flanges will be made of 2 mm of aluminum (2 % X_0). The honeycomb chamber will be mounted on the TPC inner wall as shown in Fig. 2.2.3. As indicated above, the layout for the front-end electronics, cables and cooling for vertex detector, forward-tracking detectors and intermediate tracker must be planned carefully so as not to place too much material in the path of the Bhabhas used for measuring the luminosity spectrum.

The choice of the cell size has to be optimized as function of resolution necessary and the amount of material. With a cell size of 10 to 15 mm and readout via multi hit TDCs at each end of the tube, the track coordinates will be determined with an accuracy of about 100 μm in the drift direction and about 1 cm along the wire.

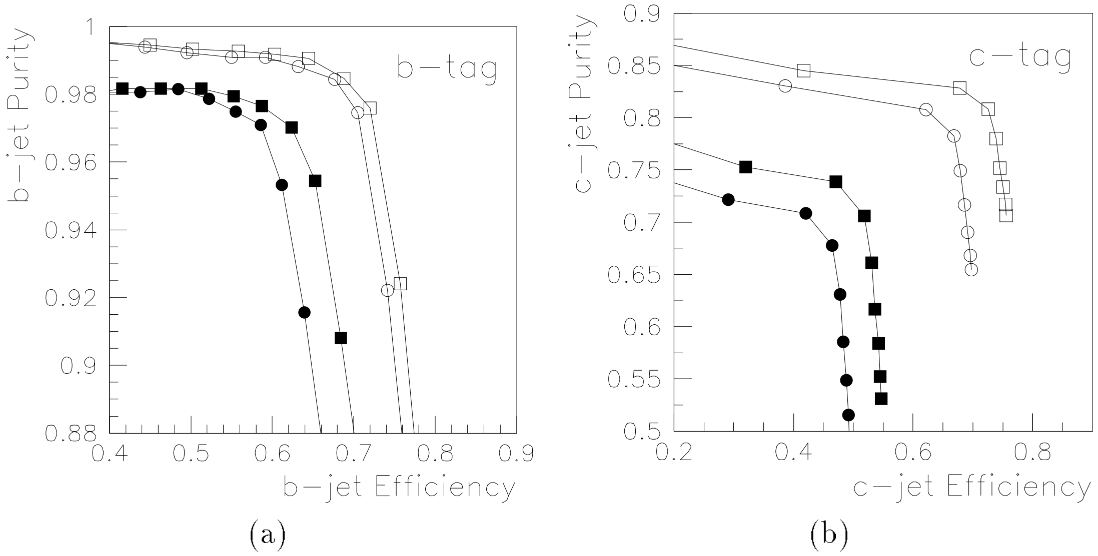

Figure 2.2.2: *Purity vs efficiency for (a) beauty and (b) charm identification in* 50 GeV *jets. Open squares and circles refer to the CCD option, with respectively* $r_{\mathrm{beampipe}} =$ 10 *and* 22 mm. *The filled squares and circles refer to the APS option for the same* r_{beampipe} *values.*

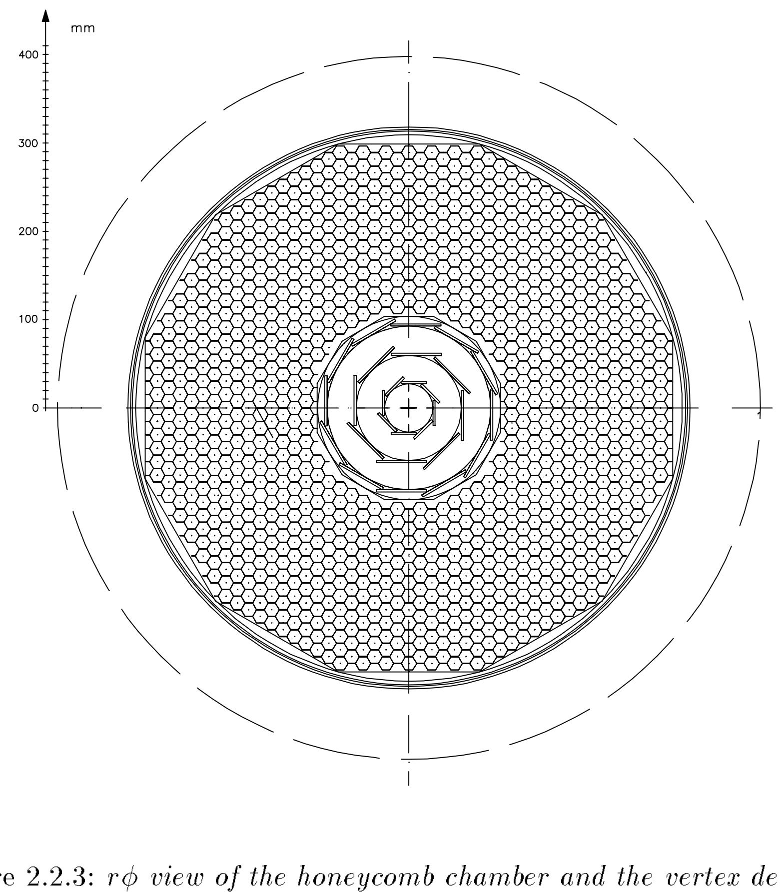

Figure 2.2.3: $r\phi$ *view of the honeycomb chamber and the vertex detector.*

2.2.3 Main Tracker

Several options were studied for the main tracking chamber: all-silicon tracking [40], an MSGC tracker [41], and a time projection chamber (TPC) [42]. The TPC was chosen as the first option in the design of the LC detector because of the excellent performance experienced at LEP [43, 44], where it proved its good momentum resolution, simple and efficient pattern recognition of complex events, and good particle identification.

2.2.3.1 The Time Projection Chamber (TPC)

The choice of a TPC is based on the experience gained in the PEP-4, TOPAZ, DELPHI and ALEPH [43] detectors and on calculations related to robustness in the background environment at the linear collider. In the following exercise, an extrapolation of the ALEPH TPC design is described, and possible areas of improvement resulting from further R&D are pointed out. The TPC offers several advantages.

- It has extremely high tracking redundancy and granularity which are important for the multijet physics at the linear collider.
- It gives good particle identification via the dE/dx ionization loss of the charged particles. This is important for the e/π separation to complement the performance of the electromagnetic calorimeter and improve the overall e/π separation to below 10^{-3} in the momentum range 1 to 50 GeV/c, for reasonable π-K-p separation, and for the energy-flow measurement [43].
- The performance profits from operation in a high B-field since the electrons drift parallel to $\vec{B}$.
- Since the wires are stretched azimuthally at end-cap sectors and thus are short ($\sim$1 m), the TPC can be long in the axial direction, to enable coverage to smaller polar angle θ.
- It is easy to maintain since the endplate is divided up into small sectors which can be readily replaced or serviced in case of problems.

On the other hand,

- it has a long memory time (50 μs), an apparent disadvantage which is more than compensated for by the high granularity (circa 10^8 3D pixel elements) as shown below;
- it does require that the B-field be well-mapped, to an accuracy of better than 10^{-3}, and that the drift volume be well-monitored with laser tracks [44].

The performance of the tracking is given by

$$\frac{\delta p_t}{{p_t}^2} = C = \frac{\sigma_{\text{point}}}{0.3\mathrm{B}(R_O - R_I)^2}\sqrt{\frac{720}{N+4}} \quad \text{for} \quad |\tan\theta| > \frac{R_O}{L}$$

$$\frac{\delta p_t}{{p_t}^2} = C \times G^2 \times \sqrt{\frac{N+4}{\frac{N}{G}+4}} \quad \text{for} \quad |\tan\theta| < \frac{R_O}{L},$$

where

$$G = \frac{R_O - R_I}{L\tan\theta - R_I},$$

with R_O and R_I being the outer and inner radii of the tracking detectors, $2 \times L$ is the length (along the beam) of the main tracker and N is the maximum number of measured points of charged particles by the tracking detectors. For the LC TPC the following choices have been made: $R_O = 1.6\,\mathrm{m}$, $R_I = 0.4\,\mathrm{m}$, $L = 2.5\,\mathrm{m}$, $N = 118$ and $B = 3.0\,\mathrm{T}$. With $\sigma_{\text{point}} \simeq 160\,\mu\mathrm{m}$ (see below), $C = 2.8 \cdot 10^{-4}$ for the TPC alone. For the ALEPH TPC alone $C = 12 \cdot 10^{-4}$, and the improvement for the LC comes from mainly the increase in B by a factor of 2 and in N by a factor of 6, which is now technologically feasible (see below).

Choosing the half-length of the chamber L to be 2.5 m means that, using the above formulae, the vertex detector + intermediate tracker + TPC will measure 200 GeV/c tracks to 30 % accuracy in the forward direction at $|\cos\theta| \simeq 0.98$, so that there is a good match to the forward tracking. This is important, for example, for the curvature measurement of muons for the determination of the anomalous couplings of the electroweak gauge bosons $\mathrm{W^+W^-}$, which are strongly forward-backward peaked. Due to the forward-peaking of $\cos\theta$, one gains rapidly in statistics at smaller angles: a factor of two in going from $|\cos\theta| = 0.94$ to $|\cos\theta| = 0.98$. The performance at small angles is even more important for other channels which will be used for the measurement of couplings and involve t-channel gauge boson fusion [45]: $\mathrm{e^+e^-} \rightarrow \mathrm{e}\nu\mathrm{W}$, $\mathrm{e^+e^-} \rightarrow \nu\bar{\nu}\gamma$, $\mathrm{e^+e^-} \rightarrow \nu\bar{\nu}\mathrm{Z}$ and $\mathrm{e^+e^-} \rightarrow \mathrm{ee\,WW}$.

2.2.3.2 Chamber Size

The chamber is situated in a 3 T magnetic field (see Section 2.1.4). The inner and outer radii of the LC TPC field cages are $\mathrm{R^{fc}_{inner}} = 0.32\,\mathrm{m}$ and $\mathrm{R^{fc}_{outer}} = 1.70\,\mathrm{m}$, and the sensitive volume of the tracking covers from $\mathrm{R^{pads}_{inner}} = 0.40\,\mathrm{m}$ to $\mathrm{R^{pads}_{outer}} = 1.60\,\mathrm{m}$. Electrons from ionizing particles drift over a length of up to $\ell_{\text{drift}} = 2.5\,\mathrm{m}$, the half-length of the chamber. Tracks can be reconstructed up to $|\cos\theta| \simeq 0.985$, using the requirement that at least four pad rows define a track.

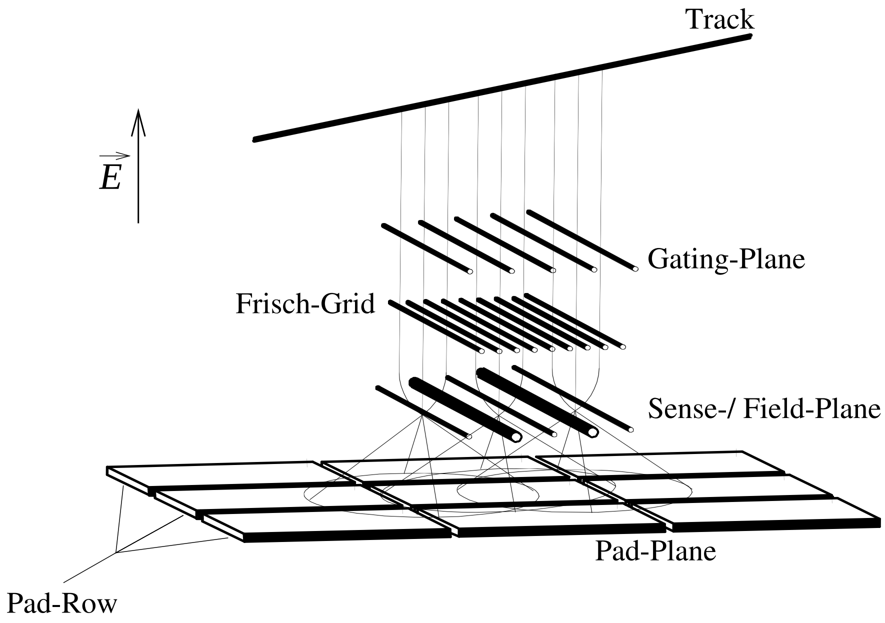

Figure 2.2.4: *Configuration for the TPC wire chamber.*

2.2.3.3 Details of the Design

The design goal is to obtain the best possible granularity by profiting from recent R&D work [46, 47]. The 3D granularity is determined by diffusion of the drifting electrons in the gas, the readout electronics and the readout-chamber technology. The relevant gas properties are the drift velocity and the longitudinal and transverse diffusion coefficients. Advances in electronics make the design of fast front-end, digitizing and buffering electronics for a large number of channels both feasible and affordable. New technologies [46, 47] for the readout chambers can also improve the granularity significantly; present possibilities are improved wire-chamber technology, micro-strip gas chamber (MSGC) [48], micromesh gaseous chamber (MICROMEGAS) [49] and gas electron multiplier (GEM) [50]. For the present, wire chamber readout technology will be studied with the gas mixture used in ALEPH to see how much the granularity can be improved. Figure 2.2.4 illustrates the configuration for the standard wire-chamber TPC readout.

Diffusion. The size of an electron cloud drifting from its point of origin to the end-cap sector is determined by diffusion in the gas. In the directions transverse and longitudinal to the drift direction, the sizes are $FWHM_T = 2.34\sigma_T = 2.34 D_T\sqrt{\ell}$ and $FWHM_L = 2.34\sigma_L = 2.34 D_L\sqrt{\ell}$, respectively, where D_T and D_L are the diffusion coefficients of the gas and ℓ the drift length. Since the electrons are drifting along the $\vec{B}$

direction, their spread is inhibited by the B-field according to $D_T(B) = \frac{D_T(B=0)}{\sqrt{1+(\omega\tau)^2}}$, where $\omega(= eB/m)$ is the cyclotron frequency and τ is the mean drift time between collisions with the gas molecules. For the gas used in ALEPH (91 % Ar, 9 % CH_4), the measured values are $\frac{\omega\tau}{B} = 5.9 \pm 0.2\mathrm{T}^{-1}$ [44], $D_T(0) = 600\,\mu\mathrm{m}/\sqrt{\mathrm{cm}}$ and $D_L = 380\,\mu\mathrm{m}/\sqrt{\mathrm{cm}}$ for a $E = 200\,\mathrm{V/cm}$ drift field, corresponding to a drift velocity of $v_D = 5.3\,\mathrm{cm}/\mu\mathrm{s}$ [46]. Thus for a 3 T B-field $\omega\tau = 17.7$, and, for a drift distance of $\ell = 250\,\mathrm{cm}$ the size of the electron cloud is $FWHM_L = 14.0\,\mathrm{mm}$ and $FWHM_T = 1.3\,\mathrm{mm}$, which translates to a volume for the 3D track pixels of $0.19\,\mathrm{cm}^3$. The volume of the TPC consists of $2{\cdot}10^9$ such 3D elements. The wire chamber readout does not exploit this fine granularity completely, as described in the following sections.

Wire chambers and pad structure. In Fig. 2.2.5, the pad structure of the TPC end plates is shown. The pads are arranged in circular rows of radial size $\Delta R = 10\,\mathrm{mm}$ and cover the entire end-plate. The pads are 2 mm wide azimuthally and the pad-to-wire distance 1 mm, corresponding to a pad-response-function width of approximately $\sigma_{\mathrm{prf}} = 1.4\,\mathrm{mm}$ [46]. (The pad response function is the form of the pulse height along a pad row induced by electrons arriving at a sense wire above.) Thus the point measuring accuracy is $\sigma_{\mathrm{point}} \simeq \sigma_{\mathrm{prf}} \times 1/\sqrt{N_{\mathrm{primaryelectrons}}} \simeq 140\,\mu\mathrm{m}$ for $N_{\mathrm{primaryelectrons}} \simeq 100/\mathrm{cm}$. There are 506 k pads in 64 pad rows in the outer sectors and 214 k pads in 54 pad rows in the inner sectors. The inner sector boundaries are arranged such that they do not point to the beam line, as shown in Fig.2.2.5, in order to have full hermeticity for the central tracking up to $|\cos\theta| \simeq 0.985$.

Electronics. The electronics can be designed such that they do not cause deterioration of the two-track resolution in the direction along the electron drift. By choosing analogue electronics with 100 ns shaping time and a clock rate for the drift-time digitization of 50 ns (giving 1000 time buckets during the $50\,\mu\mathrm{s}$ drift time for each pad), the arriving signal is broadened by the shaper by 7 % to 280 ns and is sampled six times. The information from each pad channel would be stored in a buffer, and via multiplexing of a few thousand pad channels, the number of electronic cables is reduced so as not compromise the hermeticity of the detector.

The readout granularity. As shown above, the size of an electron cloud which has drifted the full length is $FWHM_L = 14.0\,\mathrm{mm}$ and $FWHM_T = 1.3\,\mathrm{mm}$. The wire chamber readout does not capitalize completely on this fine granularity in $r\phi$ ($FWHM_T$) because the transverse readout dimension is given by in ϕ the $FWHM$ of the pad response function which is 3.3 mm and in r by the the pad height which is 10 mm. Longitudinally, the granularity will not be compromised by the readout as just explained. Thus for the readout including diffusion, the 3D volume element is $0.46\,\mathrm{cm}^3$ (ALEPH: $4.7\,\mathrm{cm}^3$) giving a total of about $7.9{\cdot}10^7$ 3D readout elements.

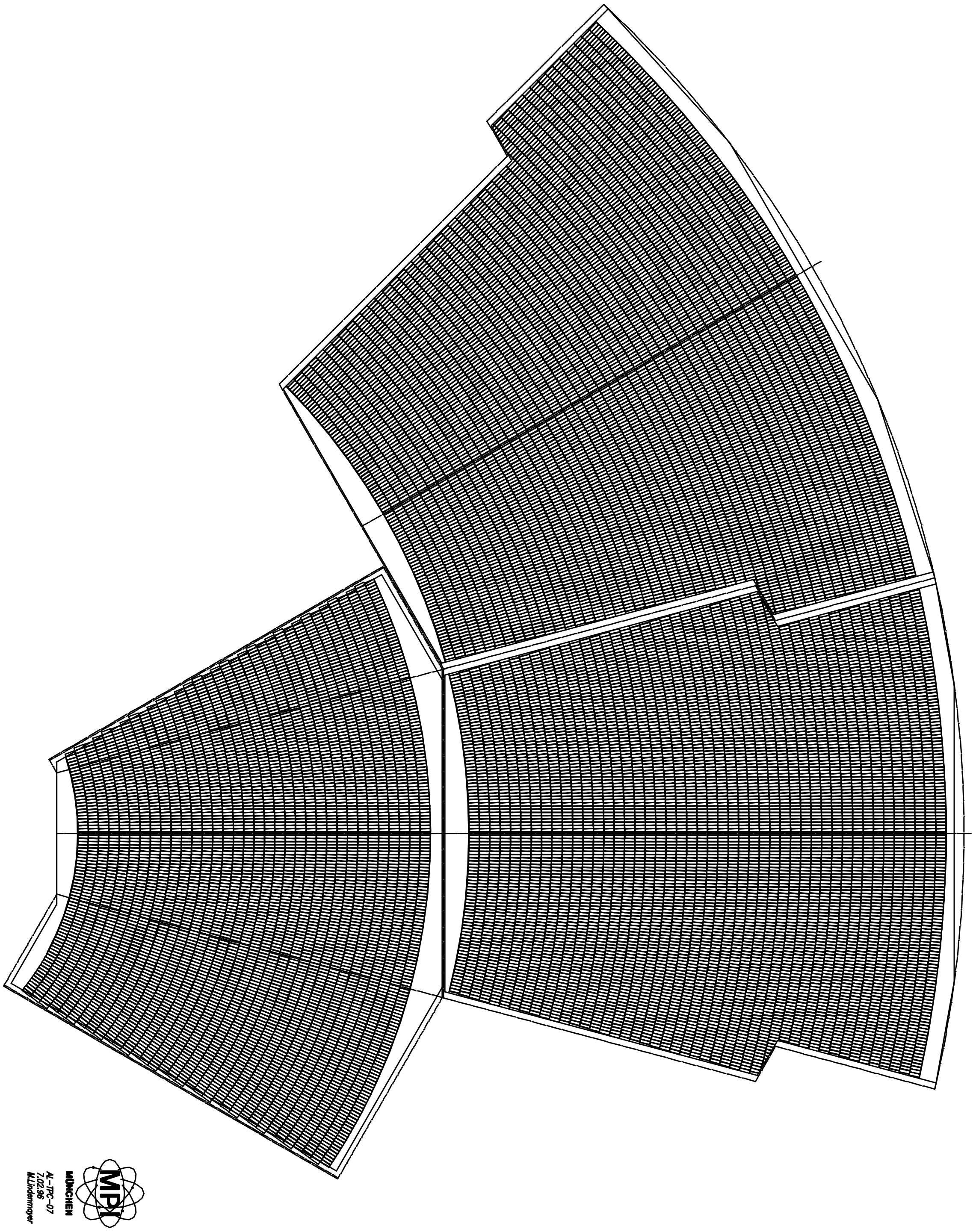

Figure 2.2.5: *TPC sectors with pad structure. The inner sector boundaries do not point to the origin.*

The dE/dx measurement and wire readout. In the ALEPH TPC, the track coordinates are measured using the pads, and the dE/dx for particle identification is measured using the signals from the wire readout. In the heavy ion experiment NA49 [51] the wires are not read out, and the dE/dx measurement is also derived from the readout of the 40 mm long pads. For the LC TPC both options are open, but it seems best to include the wire readout in the design, because then the pad and wire information can be combined to improve the coordinate measurement, the two-track resolution, the dE/dx measurement and the overall granularity, adding about $2{\cdot}10^6$ volume elements to the above figures.

Triggered gating. To reduce the background currents and positive ion build up in the TPC volume, the chamber can be operated in the triggered gating mode, by which the gate of the TPC is opened only once a good trigger is signaled. The trigger signal should arrive within $2\,\mu$s after the bunch crossing, and the final trigger rate should be less than about 20 Hz to keep the positive ions to a negligible level. It may be possible to operate in a free-running mode (gate always open), but this needs study to be sure the distortions can be corrected (see below).

Backgrounds and occupancy. As stated in Section 2.1.5, backgrounds arise from beam-beam effects, synchrotron radiation and muons from upstream sources. The main backgrounds are due to beam-beam effects: the creation in the bunch-bunch interaction of $e^\pm$ pairs and of photons which can scatter several times and enter the detector. The masking is designed to reduce them to an acceptable level.

It is estimated from background studies [52] that for TESLA 600 γ/bunch will cross the TPC and the average γ energy is about 1 MeV. About 2 % of the photons will undergo Compton scattering in the gas, and since the TPC integrates over 70 TESLA bunch crossings, they give rise to about 800 tightly spiraling electrons per TPC "picture". Due to the tight spiral (circa 2 mm diameter), these will be lines following the B field, each of which will affect typically 3 pads, so that the occupancy from this background will be at most 0.4 % per "picture". The background current produced per Hz of trigger rate is estimated to be 5 nA, three orders of magnitude below the operational experience ($5\,\mu$A) with the ALEPH TPC, which has been tested at another order of magnitude higher levels ($50\,\mu$A). Thus a 10 to 20 Hz trigger rate would lead to a total current of around 100 nA in the wire chamber sectors, which is small.

The situation is about the same for SBLC. The TPC integrates over a factor four more bunch crossings than for TESLA, but this is compensated by the factor four fewer γs produced per bunch due to the lower bunch charge.

The other sources of background are due to beam-beam $e^\pm$ pairs and slow neutrons which scatter out charged particles from the gas molecules occasionally. These backgrounds roughly double the figures above.

Distortions in the drift volume. Inhomogeneities of the electric and magnetic fields must be well controlled because they distort the paths of the drifting electrons. This leads to the tolerance on the B-field homogeneity of 10^{-3} (see Section 2.1.4), so that the correction for B-field distortions is at most a couple of mm. The experience at LEP [44] shows that the this tolerance can be met and that the B-field can be mapped to better than 10^{-4} and that the $\sim$mm distortions can be corrected to a few tens of μm. Also this experience [53] indicates that with a good field map and the $\sim 10^6$ calibration Z events from Z-peak running, even larger B-field inhomogeneities can be handled reliably. This may be necessary for the SBLC because of the compensating solenoids surrounding the final quadrupoles.

Similarly, the LEP experience has shown the field cage can be built to keep corrections for the drift-field distortions to a negligible low level. The positive ion build up also distorts the E-field and is controlled by gating, as described above. Even here, both the DELPHI [54] and the ALEPH [55] TPCs have been operated for short periods with open gate for hardware reasons, and the effects due to the positive ions were evident but correctable. These distortions could appear if it is necessary to run at very high rates (e.g. if SUSY exists and the $\tilde{\chi}^{\pm}_j$-$\tilde{\chi}^0_i$mass difference is small) so that the gate is always open. For that case as well as for the general tracking alignment, a battery of laser tracks criss-crossing the TPC volume can correct these effects.

For the ALEPH TPC [53], the Maxwell equations for the various sources of distortion were solved and introduced into a χ^2 fit to the Z-peak data with only a very few parameters per distortion. Using these fits one is able calibrate the distortions to high accuracy and control them from year to year to a level of less than $30\,\mu$m.

Underlying events. The long memory time of the TPC does not cause a problem with underlying events, because the tracks from two bunch crossings are well separated due to the $5\,\mathrm{cm}/\mu\mathrm{s}$ electron drift velocity (or more for other gases, see below), giving a $300\,\mu$m for SBLC and 35 mm for TESLA. Thus for TESLA the situation is excellent. Even for SBLC the separation is an order of magnitude larger than the reconstruction accuracy for the primary vertex by the vertex detector and is about the same size as the bunch length. It would be easy to resolve tracks from interactions separated by two or three bunch crossings. Thus the probability for an underlying event of the kind referred to in the row labeled "Minijet ev./bunch, $p_T^{\mathrm{min}} = 3.2\,\mathrm{GeV}/c$" of Tab. 2.1.7 is about 0.003 for both TESLA and SBLC.

2.2.3.4 Conclusion on Standard Technology.

In conclusion, using standard TPC technologies the granularity can be increased by an order of magnitude relative to previous e^+e^- applications by employing advances in electronics and by pushing the technology of the endcap readout wire chambers further. Nevertheless, it is worthwhile to continue R&D in the direction of improving the gas and of developing new TPC readout techniques such as MSGC [46, 47, 48], MICROMEGAS [49], and GEM [50].

As an example for improving the gas, the study for the muon collider [56], for which a TPC is considered robust enough to stand more severe backgrounds than at the LC, suggests a gas 90 %He+10 %CF_4 for which the drift velocity is about twice that of the ALEPH gas (91 %Ar+9 %CH_4) while the diffusion constants are about the same. A number of factors would give reduced backgrounds and occupancy by at least a factor two: for TESLA the memory time would sum over a factor two fewer bunches; for SBLC the vertices for two successive bunches would be separated by 600 μm; recoils from neutron scattering in CF_4 are a factor ~4 less energetic than in CH_4.

The application of the MSGC, MICROMEGAS or GEM technology for reading out a TPC for the LC detector is of great interest because they allow a reduction of the pad-response-function width and perhaps reduce the positive ion buildup around the gas-amplification region. For the MSGC, chambers with σ_{prf} between 0.6 and 1.4 mm have been built [47]; there is a complicated dependence of the gain on the strip geometry and on the bulk and surface resistivities which are the subject of continuing study. The MICROMEGAS have a conversion gap followed by a thin (about 100 μm) amplification gap above the anode plane which can be divided into pads; these two regions are separated by a 3 μm thick cathode mesh, the positioning of which is critical and needs further R&D. A possible solution is offered by GEM in which an intermediate cathode foil with a matrix of holes (of $\sim 30\,\mu$m size and $\sim 100\,\mu$m pitch) [57] is inserted between the two electrode planes and with suitable voltages provides an intermediate amplification region. R&D is necessary to understand how to build a large system using one of these technologies.

2.2.4 Combined Tracking Performance

The TPC is the main device for momentum measurements, but its performance is greatly enhanced by the inner tracking detectors, as displayed in Fig. 2.2.6. A very precise point determined by a layer of silicon microstrip detectors just in front of the TPC improves significantly the sagitta measurement, provided the detector can be aligned to reach an overall point precision of about 8 μm.

The resolution can be further improved by combining the data from all the tracking devices and imposing a beam constraint. The final resolution of $\sigma_p/p^2 = 0.6 \cdot 10^{-4}(\mathrm{GeV}/c)^{-1}$ allows a resolution on the mass of a pair of high momentum (≈ 100 GeV) muons of a size comparable with the intrinsic Z width. This resolution requires keeping the overall systematic effects in the tracking below the 10 μm level, which represents a challenge to the tracker-builders because it is a factor of 2 to 3 smaller than achieved at LEP.

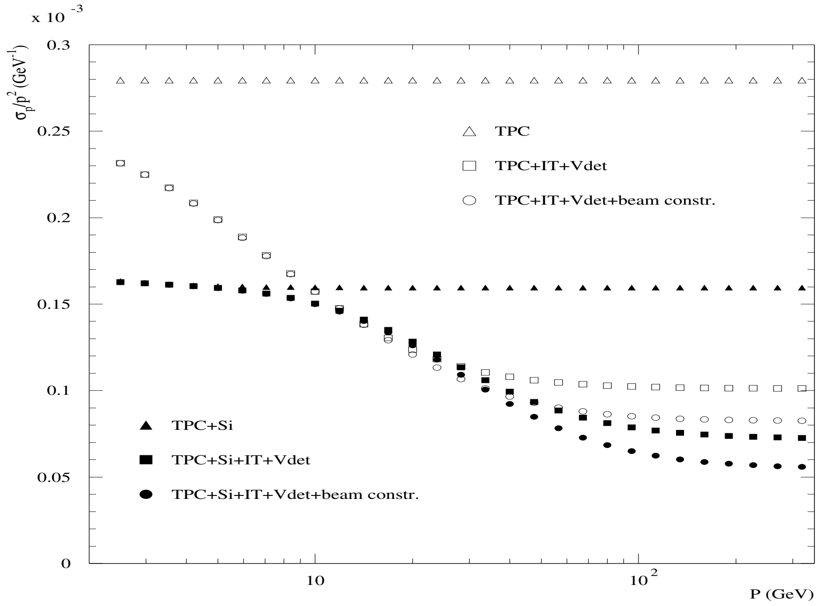

Figure 2.2.6: *Resolution of $1/p_t$ for $90°$ tracks assuming an APS vertex detector. Symbols: Vdet = vertex detector, IT = intermediate tracker, Si = intermediate silicon layer.*

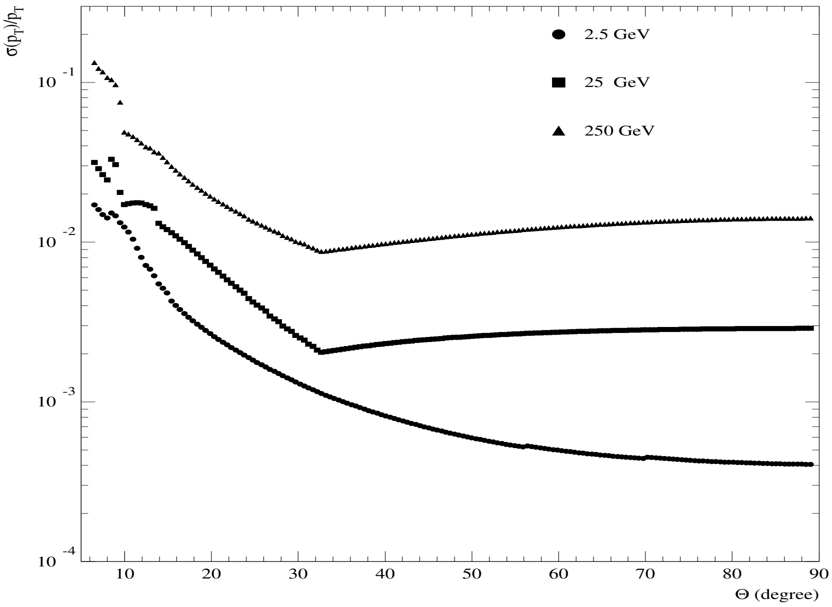

Figure 2.2.7: *Resolution of $1/p_t$ as a function of polar angle assuming an APS vertex detector.*

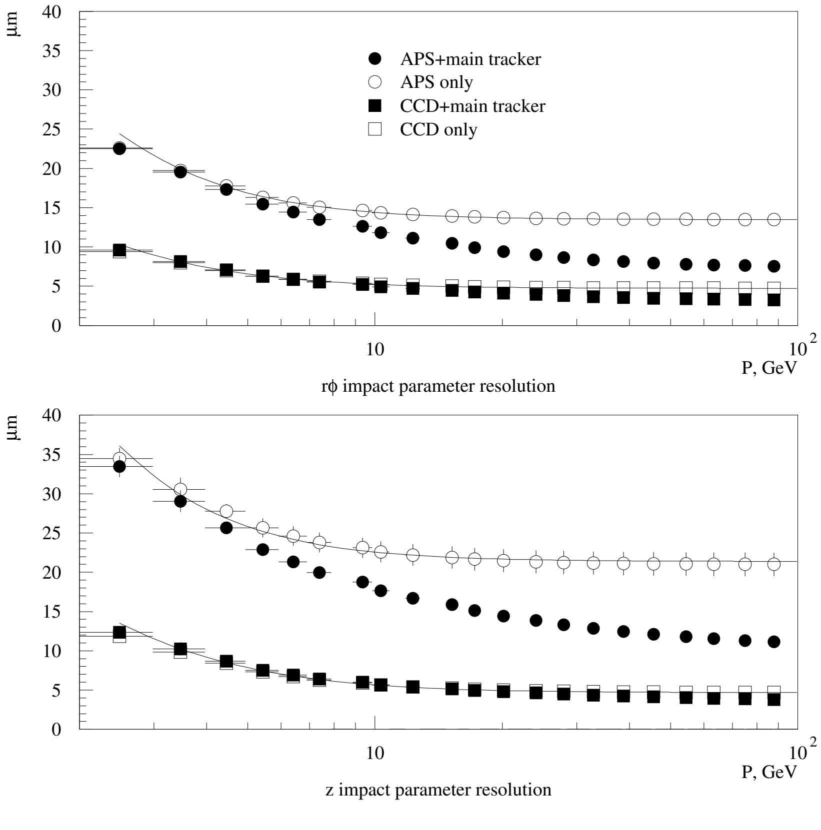

Figure 2.2.8: *Impact parameter resolution for different configurations for vertexing.*

	$\sigma_{r\phi}$ [μm]	σ_z [μm]
CCD	$4.7 \oplus 22.8/p_{\,[\mathrm{GeV}/c]}$	$4.7 \oplus 31.6/p_{\,[\mathrm{GeV}/c]}$
APS	$13 \oplus 51/p_{\,[\mathrm{GeV}/c]}$	$21 \oplus 72/p_{\,[\mathrm{GeV}/c]}$

Table 2.2.1: *Parameterization of the impact parameter resolution for the vertex detectors alone.*

At low polar angles both the projected track length and the number of TPC points decrease. It is therefore necessary to provide a precise forward tracker for momentum measurement and charge identification of energetic forward leptons. The tracking system was designed to provide a $\sigma_p/p < 30\,\%$ for tracks up to 500 GeV over the whole tracker acceptance. The performance as a function of angle is seen in Fig. 2.2.7.

The impact parameter measurement is important for the identification of decay products of short lived particles, to be used in heavy flavor tagging. Experience at LEP and SLC has shown that a gain in impact parameter measurement improves the physics capability of an apparatus (see Section 2.2.1.4). Good separation of charm from beauty requires an impact parameter resolution of at least $10\,\mu\mathrm{m} \oplus 30\,\mu\mathrm{m}/p\,[\mathrm{GeV}/c]\sin^{3/2}\theta$ in the $r\phi$ plane.

Two techniques have been studied here to achieve this performance: if the background and radiation damage rate are tolerable for very high precision CCD devices, the vertex detector can almost reach the goal with its stand-alone resolution as in the current SLD experiments at the Z peak. If the background rates exclude the use of CCDs, the APS vertex detector information can be combined with the precise TPC track information to give an impact-parameter precision for high momentum tracks of below $10\,\mu$m. The impact-parameter resolution is shown in Fig. 2.2.8. In order to compare CCDs with APSs (which have a resolution dependent on θ) an average over $30^\circ < \theta < 90^\circ$ has been performed. The impact-parameter resolution for the vertex detectors alone are determined assuming the momentum resolution of the TPC and yield the results in Tab. 2.2.1.

A benchmark for the forward tracking system was to achieve a precision for the polar angle determination of at least of 0.2 mrad for tracks below 10°. The silicon detectors proposed easily achieve this precision.

2.2.5 Calorimetry

2.2.5.1 Requirements

General. Calorimeters are used to measure the energy of charged and neutral particles. Longitudinal and lateral segmentation allows the location of the energy deposition, the identification of electromagnetic and hadronic components of the showers generated by the particles, and the identification of muons. Since dead material in front of the calorimeters worsens the resolution, it was decided to locate the superconducting coil, which represents approximately one nuclear interaction length (λ) of dead material, outside the calorimeter. The calorimeter must therefore be very compact.

Calorimeters are essential for measuring missing energy, the characteristic signature of SUSY particles and of neutrinos. Another example studied was the charged Higgs channel $H^+H^- \to c\bar{s}\bar{c}s$, for which the calorimetry is important because it is sensitive to the mass resolution of the detector. A study [58, 59] of the hadronic energy resolution has shown that the goal in Tab. 2.1.2 of $\delta E/E \simeq 50\,\%/\sqrt{E} \oplus 4\,\%$ results in a good $H^{\pm}$ detection efficiency that would not be improved much by drastically better hadronic resolution.

High resolution calorimeters. The best hadron-shower resolution is obtained in compensating calorimeters, that is, calorimeters with the electromagnetic and hadronic responses equalized, denoted $e/h = 1$. This compensation can be achieved with a U/scintillator sampling structure in which the hadronic sensitivity is increased by the nuclear fission induced by slow neutrons. For hadrons a resolution $\sigma/E \simeq 35\,\%/\sqrt{E}$ has been achieved [60]. Compensation is also achieved in lead-absorber calorimeters with resolutions of $\sigma/E \simeq 40\,\%/\sqrt{E}$ for the hadronic component and $\sigma/E \simeq 20\,\%/\sqrt{E}$ for the electromagnetic component, using a Pb/scintillator sampling ratio close to 20/5 (mm/mm) [61]. This performance results from a rather coarse-grained layer structure. A decrease of the Pb and scintillator thickness improves the electromagnetic resolution at the expense of compensation, but this degradation in compensation can be corrected for by weighting the hadronic component of the shower at the software level. This weighting technique in a multi cell Pb/LAr and Fe/LAr calorimeter [62] was shown to improve the resolution by using the iterative method described in Ref. [63]. A resolution $\sigma/E \simeq 40\,\%/\sqrt{E}$ was obtained for hadrons and $\simeq 10\,\%/\sqrt{E}$ for electrons.

The fractional resolution improves with energy as $\sqrt{E}$ but it is limited by a constant term and a noise term. The constant term dominates at energies above typically 100 GeV, whereas the noise term is important at energies around that deposited by minimum ionizing particles. To improve the resolution at high energy the constant terms will be kept as small as possible, $< 2\,\%$ for hadrons and $< 0.6\,\%$ for electrons.[1] With this performance, missing energy, a signature of new physics, can be measured very well down to a few GeV [64].

[1] These constant terms are a factor two smaller than in Tab. 2.1.2 and thus are superb goals.

2.2.5.2 Layout

Principle. The sampling thickness envisaged for the active and passive absorber layers will be kept close to that needed for compensation. However complete compensation cannot be with the electromagnetic resolution required in Tab. 2.1.2. The improved hadronic resolution due to compensation will be regained because the calorimeter granularity is fine enough to permit software energy-weighting. Good homogeneity, compactness and hermeticity can be achieved with a "Shashlik"-type tower structure in which the layers consist of a sandwich of absorber and scintillator with wavelength shifting fiber readout. The photodetectors and the readout electronics can be outside the sampling structure and cracks due to wavelength shifter layers or bars can be avoided. Such calorimeters techniques have already been tested and described [65]. They have also been proposed as an alternative to the radiation-sensitive lead tungstate crystal calorimeter for CMS [66]. Shashlik modules are also used in the STIC at DELPHI/LEP [67] and are now being built for the HERA-B detector at DESY [68].

Absorber material and thickness. For the electromagnetic section, Pb is a good candidate for the passive medium given its very short radiation length X_0. It has been observed that compensation is possible with a Pb/Scintillator sampling structure in which the volume ratio of lead to scintillator is 4/1 [60]. The LC detector will have 30 sandwich layers of 5/5 mm Pb/Scintillator sheets corresponding to $27\,X_0$, because better electromagnetic resolution at the expense of compensation is desired (see above). For the hadronic section, Cu is used because it has a short interaction length and good mechanical stiffness, which allows for smaller dimension tolerances and more precise machining. An optimal sampling structure is expected with 20/5 mm Cu/Scintillator layers. The interaction length in the hadronic section is $\lambda = 7.5\,\text{cm}$ and in the electromagnetic section $\lambda = 30\,\text{cm}$.

Calorimeter Structure

Supertowers. The building blocks of the barrel and endcap calorimeters are supertowers. The thinner Pb/Sci electromagnetic section in front is followed by the thicker Cu/Sci hadronic section. Supertowers are laterally divided into 4×4 hadronic towers and 8×8 electromagnetic towers. An overview of the calorimeter structure is shown in Fig. 2.2.9 and details are given in Tab. 2.2.2.

The supertowers have an angular width of $\Delta\theta = 3.5°$ at $\theta = 90°$ and a lateral size of $22.4 \times 22.4\,\text{cm}$ ($26.7 \times 26.7\,\text{cm}$) at the front face (end face) of the calorimeter; these dimensions are kept roughly constant over the polar angle θ. The longitudinal supertower thickness (length) is 5.4λ (114 cm) at $\theta = 90°$ and increases with θ to $\approx 8.4\lambda$ at $\theta = 30°$ and $\theta = 150°$. The weight of the supertowers varies between 600 and 850 kg.

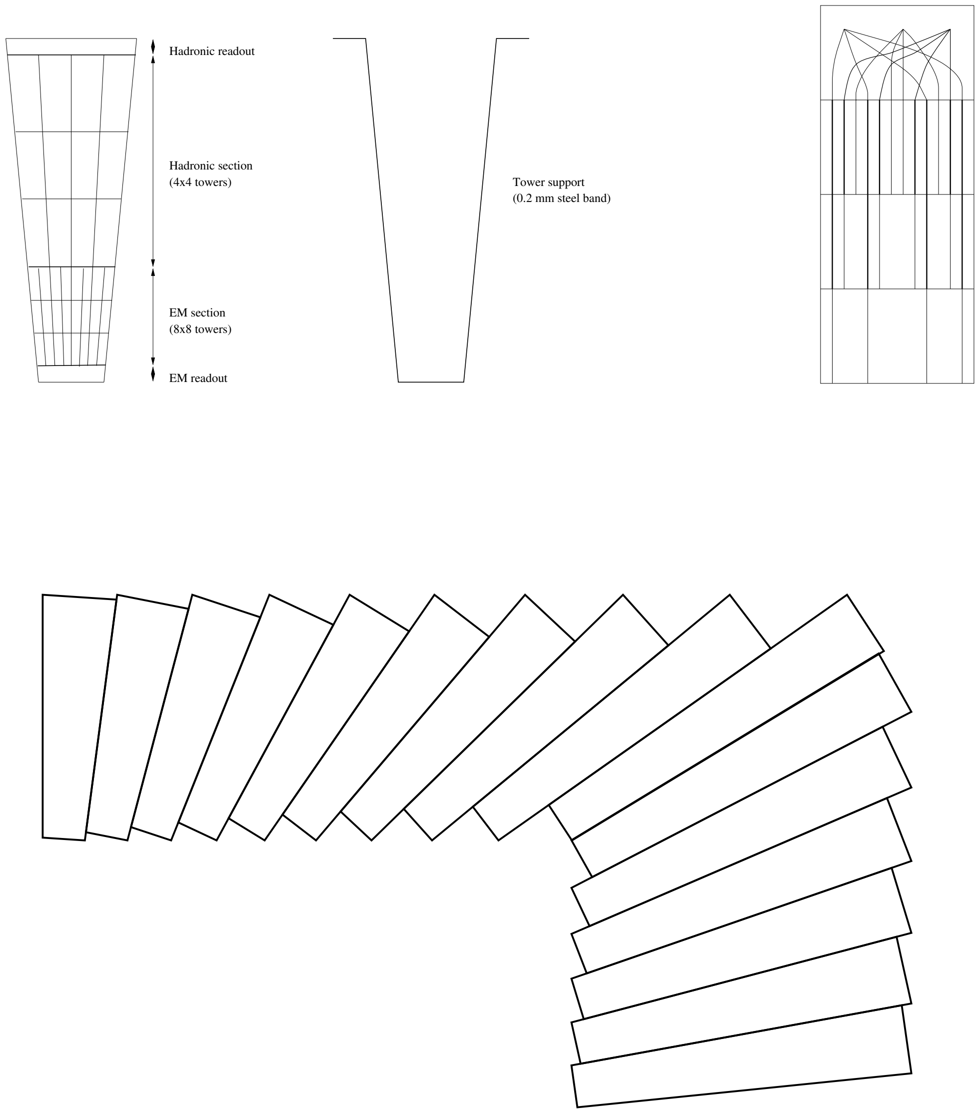

Figure 2.2.9: *Schematic drawings of a Shashlik supertower (top left), of the steel band support (top center), of the WLS readout fibers (top right) and of the arrangement of the rings of supertowers(bottom).*

Section	Radial limits (cm)	Depth (X_0, λ)	Material	Scint/Abs (mm/mm)	Number of layers	Number of longit. readout cells
Barrel						
Pre-sampler	170–172	$1.6X_0$	SciFi/Pb		2	2
ECAL	172–210	$27\,X_0$ 1.1λ	SciFi Pb WLS fib.	5/5	30	3
HCAL	210–300	4.7λ	SciFi Cu WLS fib.	5/20	33	3
Coil	300–375	0.9λ	Al Scint. pads	740/10	1	1
Tail Catcher	380–640	11λ	Fe/RP chamber	50/30 150/30	20+5	20+5
Endcaps						
ECAL	(r) 23.5–210 (z) 280–330	$27X_0$ 1λ	SciFi Pb WLS Fib.	5/5	30	3 or 4
HCAL	(r) 23.5–300 (z) 330–460	10λ	SciFi Cu WLS fib.	5/20	94	3 or 4

Table 2.2.2: *Calorimeter structure.*

Section	Angular acceptance	Number of rings	Number of super-towers	Number of readout cells	Approx. tower size (cm×cm)	Approx. tower half angle
Barrel	30°–150°	20	1000			
ECAL				192,000	2.8×2.8	0.47°
HCAL				48,000	5.6×5.6	0.94°
Coil				1,700	40×40	
TC				17,000	40×40	
Endcaps	4.85°–30° 150°–175.15°	2×6	2×174			
ECAL				66,816	2.8×2.8	0.29°
HCAL				16,704	5.6×5.6	0.58°
Grand Total				342,220		

Table 2.2.3: *Calorimeter granularity.*

Supertower rings. The whole calorimeter is made of 32 supertower rings, with 20 rings in the barrel section between 30°and 150°, and 50 supertowers making up one ring. Details are given in Tab. 2.2.3. The weight of a ring varies between 30 and 45 tons.

The calorimeter is closed by two endcaps, each consisting of 6 rings with decreasing number of supertowers down to $\theta = 4.85°$. The endcaps cover the angular range between the beam pipe and the barrel calorimeter ($4.85° < \theta < 30°$ and $150° < \theta < 175.15°$).

Supertower longitudinal sections. The outer radius of the hadronic section of the barrel calorimeter is constrained by the coil radius. The minimal depths of both electromagnetic and hadronic sections were determined by GEANT Monte Carlo simulations [69, 70]. These resulted in specifying an electromagnetic section $27\,X_0$ deep, equivalent to 30 Pb/Sci layers of 5/5 mm and a barrel hadronic section $4.4\,\lambda$ deep ($\simeq$ 84 cm.) at $\theta = 90°$. The tail catcher (see below) measures the end of the shower which leaks out through the coil.

For the endcaps, the depth of the electromagnetic section is the same as in the barrel and that of the hadronic section is $9\,\lambda$ or more. The endcap iron is also instrumented as tail catcher. The electromagnetic calorimeter starts at $z = 2.80$ m from the interaction point, and the hadronic section extends to about $z = 4.6$ m. The inner radius is 23.5 cm.

Tower sizes. The 4×4 hadronic towers in a supertower each have 5.6×5.6 cm cross section at the entrance window and cover an acceptance of 1.88° in φ and θ.

Each hadronic tower is preceded by 2×2 electromagnetic minitowers of 2.8×2.8 cm ($\Delta\theta = 0.94°$). This size is well adapted to the lateral size of the electromagnetic shower (Moliere radius $\simeq 2$ cm).

In the endcaps, the supertower and tower sizes are approximately the same as those in the barrel calorimeter. Due to the larger distance from the interaction point, the angular granularity of the hadronic tower improves to $\Delta\theta \simeq 2\ 1.2°$.

Cell segmentation. The electromagnetic section will be longitudinally segmented into at least three readout cells. To permit a good e/π separation, three cells of depths of 4, 12, and 11 X_0 can be used. For the hadronic section, longitudinal segmentation into at least three cells is also needed in order to have the information for software compensation. In the present design the hadronic towers are divided into three cells of equal depth of about $1.5\,\lambda$ ($\simeq 28$ cm); the optimization of individual cell depths will be the subject of further Monte Carlo studies.

In the endcap calorimeters, there are also three longitudinal cells for both the electromagnetic and hadronic sections at the moment. The number and depths of these cells still need to be optimized by Monte Carlo simulations.

Cracks. The energy leaking through cracks can be avoided in a design where the supertowers do not point directly to the interaction vertex. Therefore an alignment offset of 3° is built into the system. In addition, support and signal cables for the electromagnetic section will not run between the supertowers or the rings. They will be run in front of the electromagnetic section and exit the detector through two non-pointing cable slits at 30° and 150° between the barrel and endcap calorimeter.

Photodetectors. The photodetectors must be insensitive to the strong magnetic field and, in order to fulfill the calorimeter compactness requirement, must be very short. Stability and insensitivity to temperature changes are essential requirements. They are envisaged to operate in front of the electromagnetic section, where the shower development has not yet started and beyond $5.4\,\lambda$, where most of the shower energy is already absorbed. The development of vacuum phototriodes and phototetrodes [71], avalanche silicon photodiodes (AVPs) [72] and proximity focused multichannel hybrid PMTs (HPMT) [73] is progressing rapidly.

Coil Calorimeter and Tail-Catcher Sections

The superconducting coil calorimeter section is considered separately for optimization. The coil is a single absorber layer, mainly aluminum ($0.9\,\lambda$), in a 75 cm deep cryostat, and the readout being considered is one scintillator layer just outside the cryostat. Laterally it could be segmentated into pads with dimensions approximately the same as the dimensions of a supertower end face; a scintillator thickness of 1 cm should be sufficient. The light could be wavelength shifted in double-cladded WLS readout fibers and transported to photomultipliers via clear optical fibers.

The tail (a few percent) of the hadronic shower leaks out of the back of the hadron calorimeter and the coil, and the iron surrounding the superconducting coil is instrumented to act as tail catcher. A detailed description is given in Section 2.2.6. Similar tail catcher structures already exist in several large experiments, e.g. H1 [74].

Presampler

The presampler improves the measurement of electron and photon lateral position, π^0 reconstruction and e/γ separation. The present idea is to use two superlayers of fibers sandwiched with $1.6\,X_0$ of Pb. Each layer would consist of 10^5 radiation-hard, double-cladded blue scintillation fibers of 1 mm diameter, arranged in stereo layers and running roughly parallel to the beam. The inner superlayer would be made of six staggered layers of 10^4 fibers each, with a pitch of 1.07 mm, and would give an $r\phi$ resolution of $50\,\mu$m. The outer superlayer would consist of four staggered layers and give an $r\phi$ resolution of $80\,\mu$m. The presampler would be mounted directly in front of the electromagnetic barrel calorimeter on the outer wall of the TPC, have a length of 2×280 cm and cover the polar angle range $33° < \theta < 148°$. Further details can be found in Ref. [75].

More simulation of the shower development in the magnetic field will be done to optimize the structure of the presampler and improve further the measurement of the shower energy.

2.2.5.3 Calorimeter Electronics

Signal boxes. The photodetectors and associated electronics are located at the top and bottom of the supertowers. The details of the readout depend on the choice of the photodetector and are still being specified. The monitoring of the gain of each cell can be done with LED or laser light, injected via optical fibers from outside the detector. Only one injection fiber per supertower is needed.

Trigger and readout. Calorimeter-based triggers are a key element to the Level-1 trigger and will be based on:

– total tower multiplicity,

– total electromagnetic energy,

– total hadronic energy,

– total global energy,

– energy leakage from barrel calorimeter,

– missing energy,

– missing transverse energy.

The 6 ns SBLC bunch spacing makes it necessary to use a pipeline to readout the data, the time being too short for a final trigger decision. The 708 ns bunch spacing of TESLA allows for enough time to make a reasonable trigger decision before readout.

Underlying events are a minimal problem for the calorimeter since the time resolution is approximately 1 ns, depending on the photodetectors and amplifiers used.

2.2.5.4 Performance

As mentioned in the previous sections, several effects contribute to degrading the sampling energy resolution of the calorimeter. The final resolution receives a contribution from a noise term and a constant term. The noise term includes white and coherent noise which must be kept small in order to allow a precise calibration with cosmic and halo muons. This can be achieved with the use of low-capacitance photodetectors, optimal electronic amplifier design and proper grounding. The constant term, which dominates at high energy, can be reduced by minimizing the amount of dead material in front of the calorimeter and between the supertowers and by avoiding cracks. Stable response can be optimized by keeping the temperature and the supply voltages constant, by minimizing rate effects and by permanent gain monitoring. Further reduction of the constant term can be gained by software-weighting the individual signal samples to make the e/h ratio as close to unity as possible. As other experiments have shown [76], it is possible to make the constant term smaller than 0.6 % in the electromagnetic calorimeter and smaller than 2 % in the hadronic calorimeter [77].

Calorimeter depth optimization.

Parameterized shower profiles. Several options for the structure of the calorimeter were studied; energy resolutions used were parameterization of those measured in previous experiments.

For various sampling layer structures, the intrinsic resolution was studied as a function of the global depth of the calorimeter within the superconducting coil, as well as a function of the relative depths of the electromagnetic and hadronic sections.

The longitudinal profile of a hadronic shower was parameterized as in Ref. [78]. The fraction of hadronic energy deposited in each calorimeter section was calculated by integrating the shower profile in the corresponding section and smeared according to experimentally measured intrinsic resolutions [79]. Electromagnetic showers were assumed to be fully contained in the $27\,X_0$ deep electromagnetic section of the

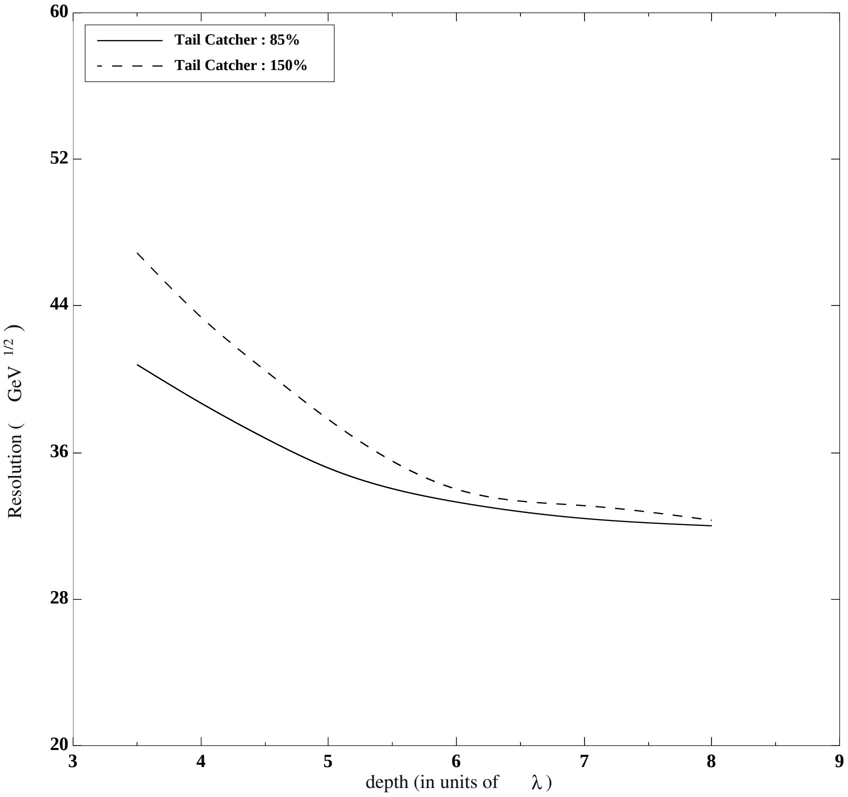

Figure 2.2.10: *Dependence of the intrinsic energy resolution $(\sigma/E)\sqrt{E}$ as a function of the depth (in units of interaction length) of the calorimeter inside the coil volume for two different tail-catcher resolutions.*

calorimeter and the energy deposit was merely smeared. To study the variation of the calorimeter performance, $e^+e^- \to W^+W^-$ events were generated with PYTHIA at 800 GeV center-of-mass energy and the energy of the particles in W jets was deposited in the calorimeter using different depths, materials, structures and resolutions. For the study, a single-particle resolution of $\sigma/E = 0.145/\sqrt{E}$ was assumed for the electromagnetic calorimeter for photons and electrons, and a hadronic resolution of $\sigma/E = 0.445/\sqrt{E}$ for the combined electromagnetic and hadronic sections. For the coil calorimeter section, a resolution of $\sigma/E = 1.5/\sqrt{E}$ was postulated. Two cases have been studied for the tail catcher: one with resolution $\sigma/E = 0.85/\sqrt{E}$ and the other with $\sigma/E = 1.5/\sqrt{E}$. Under these conditions, the resolution of the total energy of the particles in W jets was calculated for various depths of the calorimeter, the total depth being kept constant ($10\,\lambda$) for the sake of simplicity.

The jet-energy intrinsic resolutions $(\sigma/E)\sqrt{E}$ are shown in Fig. 2.2.10. Two important qualitative features are to be noted for a depth of the calorimeter inside the coil of greater than $5.4\,\lambda$. First, the energy resolution varies little as the depth increases; second, an improvement of the resolution of the tail catcher does not improve significantly the overall resolution of the calorimeter. It follows from these simulations that the depth of $5.4\,\lambda$ proposed in this report is sufficient from an energy resolution standpoint. More details about these simulations can be found in Ref. [69].

GEANT simulation. The second more detailed approach [70], relies on a complete GEANT simulation of the electromagnetic and hadronic shower development in a calorimeter similar to that discussed above. Results are obtained for the energy resolution for electrons (3 to 100 GeV), positive pions (3 to 100 GeV) and W jets generated by PYTHIA. The energy range covered by the W jets is 10 to 200 GeV. The particles and jets are assumed to hit the calorimeter at normal incidence and the dead material in front of the calorimeter consists of the beam pipe and the TPC. In what follows, results are presented for a $5.4\,\lambda$ deep calorimeter, including the electromagnetic section. Electromagnetic showers are completely absorbed in the nearly $27\,X_0$ deep lead-scintillator calorimeter section.

Pions deposit little energy in the electromagnetic section on average, since the latter is only $1\,\lambda$ deep. The energy resolution is determined by the structure and the depth of the hadronic section of the calorimeter. For a full containment of the shower, the coil calorimeter layer and the tail catcher are necessary. Figure 2.2.11 shows the calorimeter response to 30 GeV single pions for two cases: one in which only the calorimeter is taken into account and one in which all sections are included (i.e. calorimeter, coil calorimeter and tail catcher). Without the coil calorimeter and tail catcher, the measured pion energy is on average 28.7 GeV, with an RMS of 4.8 GeV, the distribution showing a long tail at lower energies. In contrast, the inclusion of the tail catcher and the coil layer increases the mean measured energy to 29.5 GeV and reduces the RMS down to 3.7 GeV, corresponding to a relative resolution of about 13 %. Energy fluctuations larger than 10 GeV are observed only at the 0.1 % level, fluctuations larger than 15 GeV are negligible. Such a calorimeter would allow good measurement of, and efficient triggering on, missing energy.

The electromagnetic energy resolution is shown in Fig. 2.2.12. An energy resolution of

$$\frac{\sigma}{E} = \frac{0.103}{\sqrt{E}} + 0.006$$

is possible in the absence of cracks between the towers and of noise. The relative energy

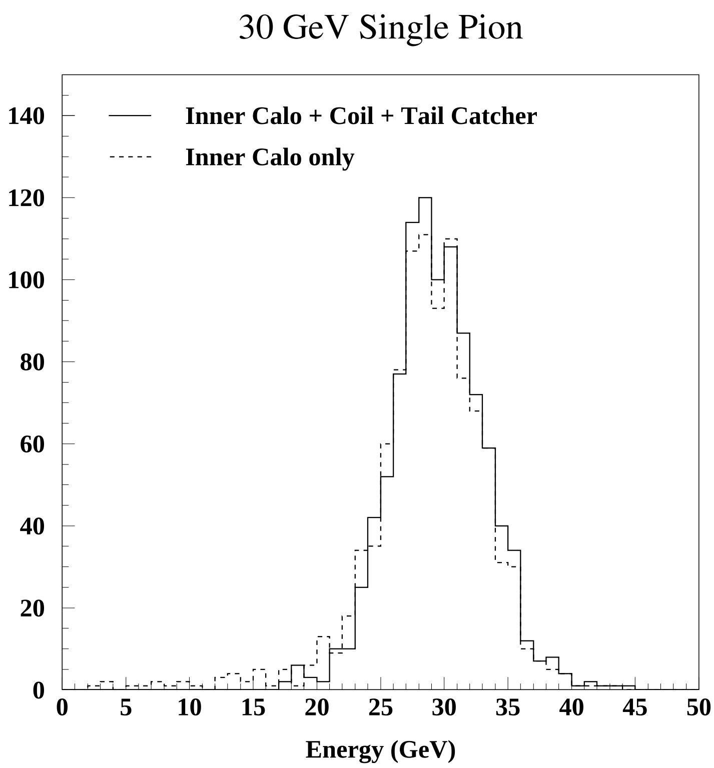

Figure 2.2.11: *Comparison of the energy deposit of* 30 GeV *pions in the calorimeter with (dashed lined) and without (solid line) the tail catcher.*

resolution for single pions can be parameterized by

$$\frac{\sigma}{E} = \frac{0.405}{\sqrt{E}} + 0.042$$

The resolution and particularly the constant term can be improved with appropriate software energy weighting which compensates for the difference in electromagnetic and hadronic response. The energy resolution for jets is given in Fig. 2.2.12 and can be parameterized by

$$\frac{\sigma}{E} = \frac{0.566}{\sqrt{E}} + 0.006$$

Fig. 2.2.13 shows the measured energy distribution of 1000 jets, all of them having an energy of 100 GeV. The average reconstructed jet energy is 99.5 GeV, with an RMS of 7.1 GeV. Seven events have a missing energy in excess of 20 GeV, three events have a missing energy greater than 30 GeV and only one event has a missing energy above 40 GeV.

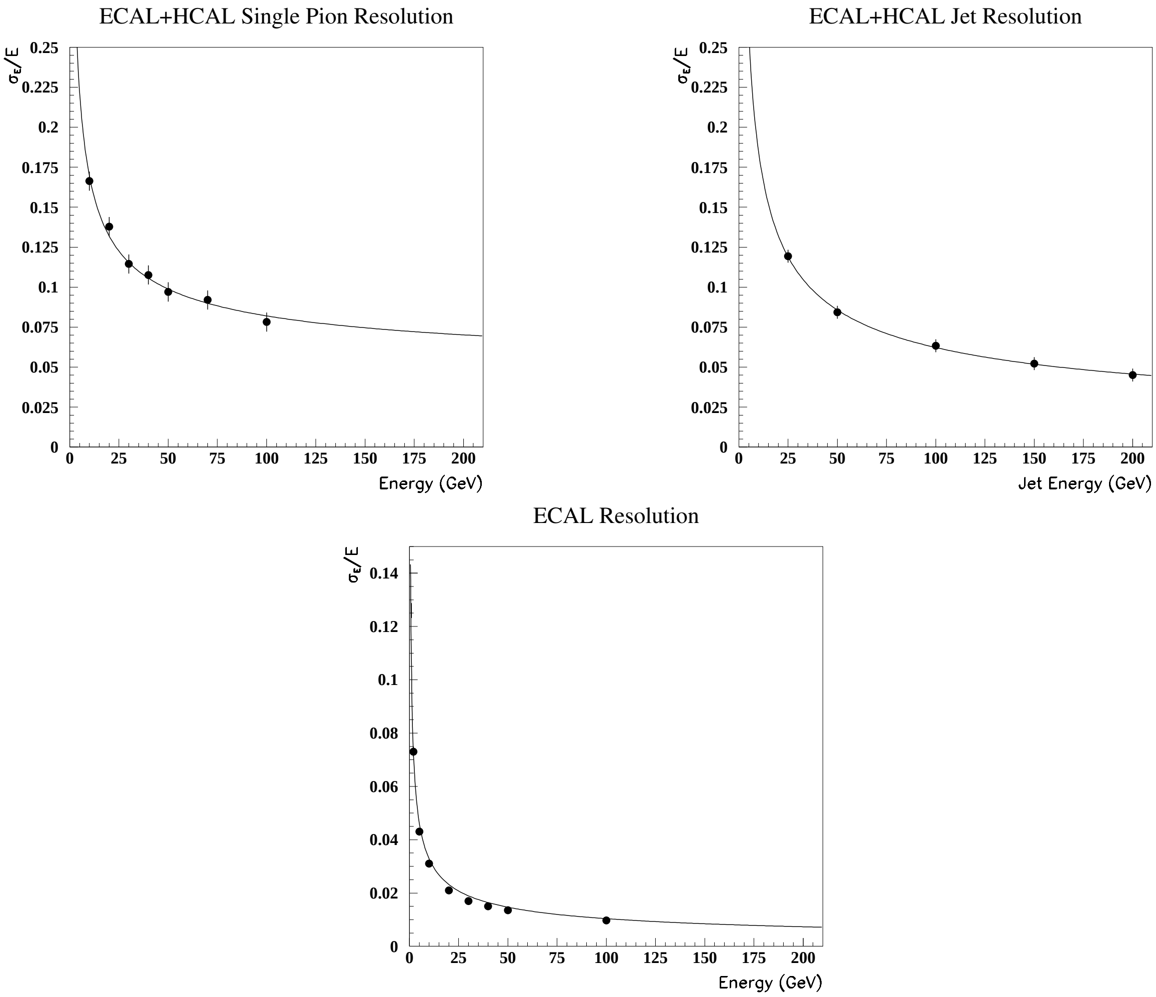

Figure 2.2.12: *Single-pion energy resolution (top left), jet energy resolution(top right) and electromagnetic energy resolution (bottom).*

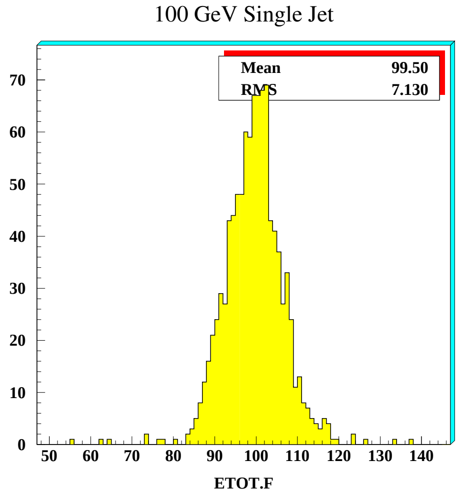

Figure 2.2.13: *Calorimeter jet energy distribution for* 100 GeV *incident jets.*

Other aspects of the performance.

Energy weighting. Energy weighting has not been applied in any of the approaches discussed above. However, this technique has proven successful in improving the energy resolution of existing calorimeters. The method was first used in the CDHS experiment [80]. The H1 collaboration at HERA applies such "software compensation" in their fine-grained Pb/LAr (electromagnetic) and Fe/LAr (hadronic) calorimeter. Results from early beam tests are described in [76, 77]. The sampling energy resolution reached is $11\,\%$ $(50\,\%)$ $/\sqrt{E}$ for electrons (pions) with a constant term of $\leq 0.6\,\%$ $(2\,\%)$ for electromagnetic (hadronic) showers. The jet-energy resolution is $44\,\%/\sqrt{E}$ and can be improved for jets having a large electromagnetic fraction [63]. The improvement which can be gained by applying such weighting methods for the proposed structure will be studied by Monte Carlo simulation in the near future.

Energy flow. The main aim of an energy flow reconstruction algorithm is to provide the energy and the directions of hadronic jets. Two approaches to date have been (*i*) a purely calorimetric method, as generally used in pp or ep colliders, and (*ii*) a method that exploits all subdetectors and particle identification capabilities, as used for example by ALEPH[81].

The present LC detector has been designed assuming method (*ii*) will be used. The charged particle momenta are measured by the tracking to determine the energy and directions of all charged particles. Low-to-medium energy jets have usually a large enough spatial spread to give rise to well-separated calorimeter clusters originating from the particles in the jets. The calorimetric energy deposited by identified muons and electrons can be isolated due to the fine transverse granularity of the calorimeters. Photons in jets can often be identified via their characteristic transverse shower profile. Similarly for isolated neutral hadrons (i.e., ones not linked to the extrapolation of a charged particle track): the fine transverse granularity of the calorimeter and the high magnetic field allow neutral hadrons to be identified if their clusters are separated. For isolated particles, the energy measurements from the tracking and the calorimeters can be combined for an improved measurement. Finally, the four-momenta of all particles thus detected are used in jet-clustering algorithms.

The total energy-momentum conservation in e^+e^- collisions can be used to constrain the jet energies, and for this the jet directions play a major rôle since they are usually measured better than the jet energies. Due to the magnetic field, the charged particles that reach the calorimeter deposit their energies at angles quite different from the original particle directions. This degrades the jet angular resolution for the purely calorimetric method (*i*), while method (*ii*) corrects for this effect. In ALEPH typical values for the jet angular resolution are 35 mrad for method (*i*) and 18 mrad for method (*ii*). For the LC detector, the measurement using method (*i*) will be dominated by the spreading by the magnetic field, while method (*ii*) should be much improved with respect to ALEPH.

Method (*ii*) has been shown [81] to give better results than method (*i*) for measuring jet directions because it includes the curling low momentum charged particles that do not reach the calorimeters and the muons which cannot be measured calorimetrically; these are two important losses in the calorimetric method (*i*).

Further simulations with the present set-up are needed to optimize the energy flow algorithm and measurement, especially in light of the superior performance of the calorimeters and the higher jet energies at the LC compared to LEP1. For example, careful studies of the calorimeter must be done to minimize the loss of resolution due to neutral particles having clusters that overlap with other clusters in the calorimeter and due to the broadening of the calorimeter showers in the magnetic field. Then, in the barrel region, the tracker dominates the energy measurement, while in the endcap below polar angles of about 0.4 rad the tracker resolution gets worse and the calorimeter dominates, and studies will help understand and improve the energy flow measurement in this transition region. Other points to optimize are the tower size, cracks between towers, longitudinal segmentation and software compensation, the coil calorimeter and tail-catcher sections, the particle identification via dE/dx and kink recognition in the tracking, the transition region between barrel and end-cap in trackers and calorimeters, the transition region between main tracker and forward tracker, to mention a few.

Clearly how to handle the jet-jet resolution problem is one of the lessons being learned right now at LEP2 and is more difficult than most people imagined. Thus is a reason for the emphasis on better energy-flow tools for the LC detector.

Angular resolution. The proposed cell sizes at the entrance to the towers are $2.8 \times 2.8\,\mathrm{cm}$ ($5.6 \times 5.6\,\mathrm{cm}$) for the electromagnetic (hadronic) calorimeter, as described earlier. From simulation studies and measurements with similar cell sizes a resolution in $\sigma_{r\phi}$ of $\sim 4\,\mathrm{mm}/\sqrt{E} + 1\,\mathrm{mm}$ can be expected [82], leading, for energies $\geq 10\,\mathrm{GeV}$ to an angular resolution of ~ 0.9 (0.6) mrad at 90° (170°). Presampling with 1 mm fibers improves the resolution to $\sim 50\,\mu\mathrm{m}$ [75].

The angular resolution for hadronic jets is dominated by the large cluster width of the individual showers. However, combining tracks and clusters, as described in the previous section, can improve the jet angular resolution. Again, more Monte Carlo studies are needed to quantify the improvement.

e/π separation. For the reconstruction of certain final states, it is vital to have the best possible pion and electron identification. For this purpose, information about the spatial shower development, both laterally and longitudinally, must be used, and this in turn requires a very fine cell granularity to allow for a good measurement of the first and second moments of the shower shape.

The H1 liquid-argon calorimeter has a sampling structure very similar to that proposed here and gives a rejection power for 30 GeV pions of 2 to $5 \cdot 10^3$ with 95 % of the electrons being correctly identified [83]. Further improvement of the electron identification by a factor of 2 to 4 can be achieved with the 1 to $2\,X_0$ thick presampler [75]. A similar factor can be gained using the dE/dx information from the TPC [43].

2.2.5.5 Calibration and Monitoring

The absolute energy measurement and resolution achievable with the calorimeter are strongly dependent on the absolute precision of the energy calibration and the stability of the relative gain monitoring. Approximately 300,000 cells must be

- calibrated,
- adjusted in response relative to each other, and
- the e/π-response measured as a function of the angle of incident particles.

Whereas rough energy calibration values are sufficient for online performance, monitoring and trigger thresholds, precise calibration constants for the electromagnetic (hadronic) calorimeter have to be determined to an accuracy of better than 0.6 % (2 %). The calibration measurement has to be performed before installation and must be monitored closely during operation.

In addition to extensive measurements at a high-energy test beam, it is proposed to use a cosmic-muon test facility for the calibration of the assembled rings before installation. The energy deposit of a minimum-ionizing particle is approximately

40 MeV/cm(10MeV/cm) in the electromagnetic (hadronic) sections and has to be corrected for the incidence angle of the muon track traversing the cell. The determination of the e/h ratio should be done with medium-energy pion beams (up to 30 GeV), but the required precision in the knowledge of the calibration constants implies using a tail catcher calorimeter in order to tag and correct the energy leakage. The measurement of the electromagnetic response in the 3-cell deep hadronic sections requires electrons of an energy of about 6 GeV with an impact angle of 20 to 30°. The effect of the magnetic field would have to be studied using Monte Carlo simulations. These measurements and studies should permit the determination of the calibration constants including the crack effects with the required precision.

During operation of the experiment, minimum-ionizing cosmic and halo muons are always present. Using special triggers they could be recorded for continuous calibration and gain-stability monitoring.

The online electromagnetic calibration is more difficult to carry out, the rate of hard-scattered electrons being very low. Low energy neutral pions, could be used via their decay into two photons. Very good calibration conditions could be obtained from a dedicated run at the Z pole, from which at least $2{\cdot}10^6$ Z events are expected. Other possibilities for calibration include using radiative-return events and track-cluster comparisons. The latter approach would work well only in the case of well-separated clusters, and this within the limits imposed by the steeply falling transverse momentum distribution.

Gain variations resulting from temperature, power supply or amplifier drifts, aging or radiation damage of the optical components of the calorimeter, as well as rate or pedestal effects can be monitored by an external pulsed LED or laser calibration system. The stability of the light sources has to be monitored with a precision better than 1 %. The light can enter the detector via a few flexible and radiation-hard quartz fibers which have an attenuation length of several meters. The comparison of the response of each cell with the calibration light source signal would permit the monitoring of the gain.

2.2.5.6 Construction, Assembly and Installation

The electromagnetic and hadronic cells are combined into supertowers. These supertowers are assembled as one unit, with individual tiles of absorber and scintillator whose sizes increase with depth. The 2 cm scintillator tiles are tailored to the tower dimensions. (As an alternative, the lateral resolution envisaged is achieved with tiles having the dimensions of the whole supertower cross section but with a shorter – a few cm – attenuation length). The individual scintillator cells are mirror-coated before assembly. During assembly, the position of the scintillator and absorber tiles can be fixed by insertion of stiff steel fibers in 1 mm diameter pre-drilled holes for the WLS readout. The fiber density needed is approximately 0.5–1 fiber/cm^2. Prototype tests have to be carried out to optimize the resolution. The WLS fibers collect light from the corresponding calorimeter cell. The fibers are mirror-coated and blackened where they traverse the neighboring cells (Fig. 2.2.9.)

The assembled supertowers are machined and polished to 0.1 mm tolerance and wrapped in reflector foils to ensure light tightness. This way, inhomogeneities in the structure and cracks can be kept very small.

The front and back absorber plates of a supertower carry the photodetectors and the readout electronics for the electromagnetic and hadronic towers. The supertower is held together by a 0.2 mm stainless steel band (see Fig. 2.2.9) which also allows handling, transportation and installation. The supertowers are inserted into 6 m diameter cylinders made of stainless steel which can be rotated during assembly. In the endcap calorimeters, the installation of the supertowers is much easier and can be made in 1/4 or 1/2 disks. This is helpful, since the weight of these supertowers is larger than that of the barrel supertowers. After installation of the supertowers, the signal boxes can be installed and tested.

2.2.5.7 Future Studies

Further research and development must be undertaken to answer questions which have not yet been addressed. These include

- the improvement of the energy resolution of the electromagnetic section by an optimized choice of sampling and/or crystals,
- the investigation of software weighting to achieve good compensation,
- the optimization of the calorimeter cell sizes with respect to compensation,
- the study of readout performance and lateral resolution of scintillator layers with reduced light attenuation length,
- the optimization of WLS readout fiber density (between 0.2 and 2 fibers per cm^2),
- GEANT Monte Carlo simulations to optimize the cell granularity for very high energy jets (up to 1 TeV) in the forward region of the endcap calorimeter,
- further development of photodetectors,
- study of calibration monitoring.

2.2.6 Instrumented Iron

The iron return yoke, as shown in Fig. 2.2.14(a), is instrumented to supplement calorimetric measurement of hadronic energy flow and to allow the detection and identification of penetrating muons over the polar angle range $4° < \theta < 176°$ and the entire azimuth. As the return yoke is preceded by the electromagnetic and hadronic calorimeters and the superconducting coil, a total of about six interaction lengths of material, the hadronic energy deposited in the tail catcher is not large. Calorimetric measurements with accuracy $\Delta E/E \sim 0.85/\sqrt{E}$ (E in GeV) are thus adequate. They may be used in two ways:

- to improve the energy flow measurements in all events in which there is hadronic energy;

- to identify a sample of events in which no energy leaked through the hadronic calorimeter, allowing the most accurate possible measurement of hadronic energy.

The identification of high momentum muons allows the study of much interesting physics. It is thus important that the instrumented iron provide highly efficient muon identification for muons with a momentum greater than about 5 GeV. In general, the determination of the charge and momentum of these muons may be done accurately in the vertex and inner tracking detectors and in the TPC; no independent measurement is necessary within the iron. Hence, while the accuracy of measurements in the iron must be sufficient to allow unambiguous association of penetrating muons with tracks in the central tracking system, it does not need to reach the precision necessary for momentum measurements. An accuracy of the order of 1 cm in two coordinate directions is adequate. Higher accuracy instrumentation of parts of the end-cap regions is foreseen to facilitate the determination of muon charge and momentum using accurate tracking through the end-cap iron. This includes accurate measurement at the inner face of the end-caps in order to use optimally the available lever arm for muon charge and momentum determination before the muons enter the iron. Toroidal spectrometers surrounding the beam pipe outside the iron end-caps permit the study of muons at the extremes of the polar angular range.

A further requirement is that the muon system provide a trigger signal. This has two uses, firstly to indicate the presence of a muon with high momentum during the physics operation of the detector and secondly to provide a cosmic ray trigger to facilitate calibration and testing. As aspects of the instrumentation of the barrel and end-cap sections of the yoke are different, they are considered separately in the following.

2.2.6.1 Barrel

The barrel section of the iron return yoke is dodecagonal in shape, that is, it has twelve-fold symmetry. The total thickness of the iron is 180 cm. Experience at the LEP [43, 84, 85] and HERA detectors [86] and at the SLD [87] has shown that the required energy resolution can be obtained in a calorimeter with iron as passive material if sampling is done about every 5 cm (the interaction length of iron, λ_{Fe}, is 16.8 cm). However, it is not necessary to make calorimetric measurements throughout the entire yoke, which presents about $11\lambda_{\mathrm{Fe}}$ to particles at normal incidence. For muon identification purposes, adequate reconstruction of the path of a penetrating muon can be performed if the position of the muon is determined every λ_{Fe}. The yoke is therefore constructed from 20 layers of 5 cm thick iron, followed by 5 layers of 15 cm thick iron and a final layer of thickness 5 cm.

The measurement of the hadronic energy deposited in the iron and the tracking of muons is done using resistive plate chambers (RPCs) [88]. These are inserted in 3 cm wide slits between the iron layers. In addition, two layers of RPCs are inserted between the cryostat housing the coil and the iron, providing calorimetric readout and a space point on muon tracks. The following twenty slits each contain one layer of chambers. These allow for calorimetric readout and the determination of, alternately, the ϕ and z coordinates of muon tracks. The iron layer following the twentieth slit is the first which is 15 cm thick. This is followed by a slit of width 3 cm which houses a chamber instrumented to provide ϕ and z coordinates on muon tracks. This pattern is repeated four more times until the final 5 cm thick iron layer is reached. The last layer ensures that the outermost chamber is adequately shielded from any low energy background in the surrounds of the experiment. The above configuration, illustrated in Fig. 2.2.14, leads to a total thickness of the iron structure of 2.55 m.

The proposed RPC design is as illustrated in Fig. 2.2.14(b). Each chamber consists of two layers of bakelite between which there is a 2 mm gas gap. The outer surfaces of the bakelite are painted with a conducting graphite layer and the inner surfaces are treated with linseed oil. Adjacent to the graphite layers are printed circuit boards on the external faces of which are the readout strips or pads. These give coordinate and calorimetric information, respectively. The readout strips are of width 2.75 cm and pitch 3 cm and the pads are of dimensions varying from about $30 \times 30\,\mathrm{cm}^2$ to $60 \times 60\,\mathrm{cm}^2$. Smaller pads with digital readout have been successfully used by the E771 Collaboration [89]. Chambers required to measure space points on muon tracks are equipped with two sets of orthogonal strips, those required to provide calorimetric information and one coordinate have one pad and one strip layer. Contact with the strips is made at the edges of the chamber, that with the pads via cables running over the surface of the printed circuit boards. A PVC foil covers the outer faces of the pads and strips. Improved mechanical stability is achieved by mounting the chambers in an aluminum foam sandwich, with aluminum supports at the chamber edges. Connections

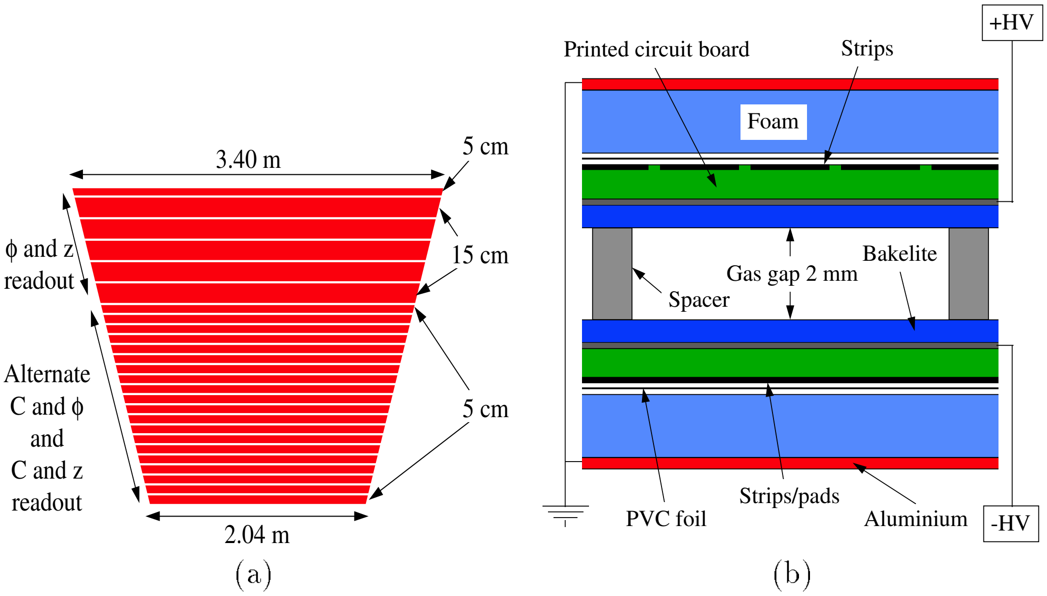

Figure 2.2.14: *(a) Cross section through one of the twelve symmetrical segments of the barrel of the iron return yoke showing the slits into which the resistive plate chambers are inserted; these are instrumented with calorimetric (C), ϕ and z readout as indicated. (b) Cross section through a resistive plate chamber.*

to the gas and high voltage supplies are made at these edges. The total thickness of the chambers is 2.2 cm.

Research is underway as to the desirability of using materials such as phenolic-melanine instead of bakelite, of increasing the size of the gas gap to about 6 mm [90], or of using a multi-gap structure [91]. The iron slits are wide enough to accommodate such chambers. In addition, tests of the performance of analogue pad readout of RPCs must be made.

The sizes and locations of the chambers are chosen to ensure that no dead solid angle is generated due to the inevitable loss of chamber efficiency around the spacers. The pad sizes and locations are similarly chosen to provide a projective tower structure matching the towers in the electromagnetic and hadronic calorimeters.

2.2.6.2 Endcaps

The instrumentation proposed for the end-caps of the iron yoke is similar to that described for the barrel, with the exception that at two depths within the end-caps the standard RPCs are replaced with chambers allowing more accurate position measurement, perhaps RPCs with finer strip pitch and incorporating ADC readout. These help determination of muon charge and momentum. Studies are still underway of the necessary chamber resolutions and best locations,which depend on the details of the magnetic field configuration in the end-caps. Further information on the charge and momentum of muons in the end-cap region is obtained using the end-cap muon tracker. This consists of two orthogonal sets of five planes of hexagonal straw tubes, similar to those described in [39] and used in the inner tracker of the LC detector. The end-cap muon tracker chambers are of width 1 cm and maximum length 3 m. High voltage and gas distribution is done at the outer end of the tubes. Readout is via TDCs at each end of the tube using electronics similar to that of the inner tracker. This allows determination of the coordinates of a muon track with an accuracy of about $100\,\mu$m in the drift direction and about 1 cm along the wire. A study is being performed of the levels of background these chambers will experience and the consequences this has for their operation. Furthermore, the possibility of using inductive strip readout to extract more accurately the position of a hit along the wire is under investigation [92].

2.2.6.3 Toroidal Spectrometers

These spectrometers each consist of a toroidal magnet sandwiched between layers of straw tube chambers. The iron magnets, similar to those used in the H1 detector [93], have inner radius 0.4 m, outer radius 3.0 m and a depth of 1.5 m. Current carrying coils are wound around the iron, producing a magnetic field of a strength of about 2 T. The hexagonal straw tubes described above are used here also, three sets of five planes of tubes, with wires at $0°$ and $\pm 60°$ to the vertical, being placed before and after the magnets. This system allows the determination of the charge of muons with momenta of up to about 250 GeV in the polar angle region given by $2° < \theta < 14°$.

2.2.6.4 Readout and Trigger

The RPC strips are read out digitally, the pads using analogue electronics. The total number of strips is about 200 000. The pad signals are summed to give a measure of the energy deposited in the inner 10 and outer 11 layers of each tower, resulting in a total number of about 7 000 channels.

A trigger signal is formed using the strip readout. Two trigger modes are foreseen. In the first the trigger logic searches for hit patterns corresponding to the signals expected from high momentum muons coming from close to the interaction point. In the second, designed for test and calibration purposes, much less stringent directional criteria are required in the trigger.

The chambers described above have a time resolution of about 1 ns. In addition to the benefits this provides when used as a trigger, either for electron-positron annihilation or cosmic ray studies, this enables rejection of halo muons using the differences between their time of arrival and those of muons from electron-positron interactions.

2.2.7 Luminosity Calorimeter

Two separate aspects of the luminosity measurement at the linear collider are (a) the luminosity spectrum measured using the forward tracking (see Section 2.3) and (b) the integrated luminosity measured using the detector described in this section. A precise measurement of the integrated luminosity will be required for the determination of the top mass from the $t\bar{t}$ cross section at threshold, as well as for the measurement of the W boson couplings from the W^+W^- cross section. The experience of the LEP luminosity monitors (luminometers) show that Bhabha scattering $e^+e^- \to e^+e^-(n\gamma)$ at very low angles should be considered as the reference process for the following reasons:

- it is a QED process and consequently the cross section can be simulated with great accuracy;

- it provides a large sample of events which can be tagged with high efficiency and purity within a well defined geometrical acceptance.

As at LEP, a calorimetric selection of the events is the best choice in order to accept radiative Bhabhas and to be less sensitive to the upstream material. Two modules (forward and backward) of the electromagnetic calorimeter can be placed inside the tungsten mask in the angular range between about 30 (30) and 55 (85) mrad around the TESLA (SBLC) beam line. The exact placement will depend on the final layout of the mask.

The small angle luminometers at LEP have measured the integrated luminosity to better than 0.1 % by establishing a well defined angular acceptance which could be simulated in very precise theoretical Monte Carlo calculations of the Bhabha cross section, including radiative corrections. There are two possible obstacles to doing a similar job for the linear collider:

i) The flood of radiation from the intersection point. It is estimated that the equivalent of 10^4 photons of 1 MeV will enter the mask at every beam crossing. Exactly where they fall, and their fluctuations, will affect the precision of measurements of the high energy showers from Bhabha scattering. The soft x-rays from the showers they produce in the inner mask may penetrate some distance into the calorimeter, distorting shower profiles.

ii) The tight geometrical constraints which may limit the containment of showers and the readout of the detector.

A radiation-hard technology exists which should enable a suitable calorimeter to be built. Considerable R&D has already been done with a view to developing a precision tracker for the LHC [94]. The calorimeter would have alternate planes of lead and of glass capillaries filled with liquid scintillator, read out via clear glass fibers to APDs

[95] or HPDs [96]. Successive planes of capillaries would be rotated by 60° to give good position resolution. The systematic precision on the inner cut-off angle for the Bhabha sample should be controllable to better than 50 microns - background radiation allowing - which would permit the integrated luminosity to be measured with comparable accuracy to that achieved at LEP. The longitudinal segmentation of the readout would allow careful systematic checks to be made of the shower reconstruction.

As well as giving the integrated luminosity, the small angle calorimeter will serve as a tagger for gamma-gamma events. It will also have an important role in completing the electromagnetic hermeticity of the whole detector down to very small angles - assuming that the tungsten mask can itself be instrumented.

Bibliography

[1] A.S. Schwarz, "Heavy Flavour Physics at Colliders with Silicon Strip Vertex Detectors", Phys. Rep. 238 (1994) 1-133.

[2] M. Adamovich et al., "WA92: a fixed target experiment to trigger on and identify beauty particle decays ", CERN/PPE 96-066.

[3] G. Bellini et al., "A microstrip vertex detector to identify heavy flavour decays", Nucl. Instrum. and Meth. A305 (1992) 395.

[4] C. Troncon, "Measurement of spatial resolution and charge collection in double sided double metal Silicon microstrip detectors", Nucl. Phys. Proc. Suppl. 44 (1995) 287-291.

[5] J. Straver et al., "1-micron spatial resolution with Silicon strip detectors", CERN/PPE 94-026.

[6] R. Turchetta, "Spatial resolution of Silicon microstrip detectors", Nucl. Instrum. and Meth. A335 (1993) 44-58.

[7] E.H.M. Heijne, P. Jarron, "Development of Silicon pixel detectors: an introduction", Nucl. Instrum. and Meth. A275 (1989) 467-471.

[8] G.D. Hallewell, "Development of active pixel vertex detectors for high luminosity particle physics applications", Nucl. Instrum. and Meth. A348 (1994) 388-398.

[9] G. Wilson, contribution to Ref. [97].

[10] M.N. Frary and D.J. Miller, in: *e^+e^--Collisions at 500 GeV: The Physics Potential, Parts A and B*, Workshops at Munich, Annecy, Hamburg, 1991, ed. P.M. Zerwas, DESY 92-123A&B (1992), p.379.

[11] C.J.S. Damerell and D.J. Jackson, "Vertex detector technology and jet flavour identification at the future e^+e^- collider", Proc. 1996 Snowmass Workshop, "New Perspectives in High Energy Physics", to be published.

[12] Proceedings of the *III International Workshop on Semiconductor Pixel Detectors for Particles and X-rays*, March 24-27 1996, Bari, Italy, to be published on Nucl. Instrum. and Meth.

[13] C.J.S. Damerell, "CCD vertex detectors in particle physics", Nucl. Instrum. and Meth. A342 (1994) 78-82.

[14] The SLD collaboration, "VXD3: the SLD vertex detector upgrade based on a 307 Mpixel CCD system", SLAC-PUB 95-6950.

[15] M. Caccia et al., "Progress in the construction of the DELPHI pixel detector", DELPHI 96-56 MVX 14, to be published on Nucl. Instrum. and. Meth.

[16] F. Antinori et al., "Experience with a $30\,\mathrm{cm}^2$ Silicon Pixel plane in the CERN experiment WA97", Nucl. Instrum. and Meth. A360 (1995) 91-97.

[17] The CMS collaboration, "Technical Proposal", CERN/LHCC 94-38.

[18] The ATLAS collaboration, "Technical Proposal", CERN/LHCC 94-43.

[19] C.J.S. Damerell, "Vertex Detectors at linear collider (Present and Future)", RAL-94-096.

[20] CERN RD19 collaboration (E.H.M. Heijne et al.), "LHC 1: a semiconductor pixel detector readout chip with internal, tunable delay providing a binary pattern of selected events", CERN/ECP 96-03.

[21] CERN RD19 collaboration (E.H.M. Heijne et al), "First operation of a 72k element hybrid Silicon micropattern pixel detector array", Nucl. Instrum. and Meth. A349 (1994) 138-155.

[22] G. Kramer et al., "Development of pixel detectors for SSC vertex tracking", SLAC-PUB 91-5518.

[23] M. Pindo, "Correlated noise in pixel detectors with analogue readout", Nucl. Instrum. and Meth. A378 (1996) 443-450.

[24] J.B.A. England et al., "Capacitive charge division readout with a Silicon strip detector", Nucl. Instrum. and Meth. 185 (1981) 43.

[25] U. Kotz et al., "Silicon strip detectors with capacitive charge division", Nucl. Instrum. and Meth. A235 (1985) 481.

[26] V. Chabaud et al., "The DELPHI silicon strip microvertex detector with double sided readout", Nucl. Instrum. and Meth. A368 (1996) 314-332.

[27] D. Schulte, private communication.

[28] A. Rudge, "Comparison of charge collection in semiconductor detectors and timing resolution using sub-ns transimpedance amplifier", Nucl. Instrum. and Meth. A360 (1995) 169.

[29] M. Menichelli et al., "Fast pre-amplifier for TOF silicon strip detectors operating in the temperature range from 20°C to −55°C", Nucl. Instrum. and Meth. A360 (1995) 177.

[30] S. A. Kleinfelder et al., IEEE Trans. Nucl. Sci. 35 (1989) 171.

[31] R. Horisberger and D. Pitzl, "A novel readout chip for silicon strip detectors with analog pipeline and digitally controlled analog signal processing", Nucl. Instrum. and Meth. A326 (1993) 92.

[32] F. Benotto et al., "The LPS trigger system", DESY 96-045, March 1996.

[33] H. Henschel et al., "A silicon backward tracking detector and trigger for the H1 experiment at the ep collider HERA", IEEE Trans. Nucl. Sci. 40 (1993) 692.

[34] B. Foster et al., "Second level trigger for the SDC silicon tracker detector", Nucl. Instrum. and Meth. A360 (1995) 325.

[35] R. Dzelyadin et al., "RD21: test of a silicon dta driven trigger processor", Nucl. Instrum. and Meth. A351 (1994) 228.

[36] C.J.S. Damerell and D.J. Jackson, SLAC-PUB-7215 (1996), to be published in Nucl. Instrum. and Meth.

[37] C.J.S. Damerell and D.J. Jackson, contribution to Ref. [97].

[38] R. Nahnhauer and M. Pohl, contribution to Ref. [97].

[39] J. F. Schottmüller, "Driftzeitmessung mit einer Wabenkammer", PITHA 94/41, unpublished Diplomarbeit (in German), III. Physikalischen Institut, Aachen University, Germany, October 1994.

[40] B. King, contribution to Ref. [97].

[41] C. Vander Velde, W. Vandoninck and F. Udo, contribution to Ref. [97].

[42] D.R. Nygren, "The time-projection chamber – a new 4π detector for charged particles", PEP Note 144, in 1974 PEP Summer Study, (PEP 137).

[43] ALEPH Collab., D. Decamp et al., Nucl. Instrum. and Methods A294 (1990) 121;
ALEPH Collab., D. Buskulic et al., Nucl. Instrum. and Methods A360 (1995) 481.

[44] The ALEPH Handbook 1995, Vol.1, ed. Chris Bowdery, ISBN 92-9083-072-7, CERN(1995).

[45] A. Miyamoto, in: *Workshop on Physics and Experiments with Linear e^+e^- Colliders, Vols.I and II*, Waikoloa, Hawaii, 1993, eds. F.A. Harris, S.L. Olsen, S. Pakvasa and X. Tata, World Scientific, Singapore, 1993, p.141.

[46] H. Wieman et al., RD-32 Status Report, CERN/DRDC 94-10.

[47] J. Bartke et al., RD-32 Final Report, CERN/DRDC 96-16.

[48] A. Oed, Nucl. Instrum. and Methods A263 (1988) 351;
A. Oed, Nucl. Instrum. and Methods A367 (1995) 34;
W.G. Gong, et al., Nucl. Intrum. and Methods A374 (1996) 144.

[49] P. Colas, contribution to Ref. [97];
Y. Giomataris, Ph. Rebourgeard, J.P. Robert and G. Charpak, Nucl. Instrum. and Meth. A376 (1996) 29.

[50] R. Bouclier et al., "The Gas Electron Multiplier (GEM)", CERN PPE 96-177.

[51] V. Eckart, private communication.

[52] D. Schulte, Ph.D. Thesis, U. Hamburg (1996).

[53] W. Wiedenmann, private communication.

[54] F. Richard, private communication.

[55] R. Settles, private communication.

[56] "Design Study for a 4 TeV $\mu^+\mu^-$ Collider",
http://www.cap.bnl.gov/~cap/mumu/book.html.

[57] F. Bartol, et al., J. Phys. III 6 (1996) 337.

[58] A. Sopczak, contribution to Ref. [97].

[59] A. Sopczak, in: *Workshop on Physics and Experiments with Linear e^+e^- Colliders, Vols.I and II*, Waikoloa, Hawaii, 1993, eds. F.A. Harris, S.L. Olsen, S. Pakvasa and X. Tata, World Scientific, Singapore, 1993, p.666;
A. Sopczak, Zeitschr. f. Phys. C65 (1995) 449.

[60] A. Bernstein et al., Nucl. Instrum. and Meth.A336 (1993) 23.

[61] E. Bernardi et al., Nucl. Instrum. and Meth.A262 (1987) 229.

[62] H1 Collaboration, Nucl. Instrum. and Meth.A386 (1997) 310;
H1 Collaboration, Nucl. Instrum. and Meth.A386 (1997) 348 and references therein.

[63] W. Braunschweig et al., Nucl. Instrum. and Meth.A265 (1988) 419;
H. Greif, Ph.D. Thesis, MPI-PAE/Exp El.229.

[64] I. Abt et al., Nucl. Phys.B396 (1993) 3.

[65] Calorimetry in HEP, BNL 1994, 177 and references therein.

[66] CERN internal note CMS TN/96-305

[67] IEE NS43 (1996) 1496.

[68] H1 Collaboration, DESY PRC-94/02, 108-117.

[69] S. Aïd, V. Korbel, contribution to Ref. [97].

[70] P. Checchia, C. Luci, M. Mazzucato, F. Simonetto, contribution to Ref. [97].

[71] OPAL Collaboration, Nucl. Instrum. and Meth.A305 (1991) 275;
CERN PPE/95-194.

[72] "CMS Technical Proposal", CERN LHCC/94-38, CMS TN/95-077, CMS TN/95-135.

[73] Calorimetry in HEP, BNL 1994, 470 and references therein.

[74] DESY H1-10/91-197, internal note; and DESY H1-2/94-344, internal note.

[75] R. Nahnhauer et al., contribution Ref. [97].

[76] H1 Calorimeter Group, Nucl. Instrum. and Meth.A350 (1994) 57.

[77] B. Andrieu et al., Nucl. Instrum. and Meth.A336 (1993) 499.

[78] R.K. Bock et al. Nucl. Instrum. and Meth.186 (1981) 533.

[79] V. Korbel, contribution to Ref. [97].

[80] H.Abramowicz et al., Nucl. Instrum. and Meth.A180 (1981) 429.

[81] ALEPH Collaboration, Nucl. Instrum. and Meth.A360 (1995) 481.

[82] T.Nicholls et al., Nucl. Instrum. and Meth.A374 (1996) 149.

[83] B.Andrieu et al., Nucl. Instrum. and Meth.A344 (1994) 492.

[84] "Performance of the DELPHI Detector", P. Abreu et al. (DELPHI Collaboration), CERN-PPE/95-194.

[85] K. Ahmet et al. (OPAL Collaboration), Nucl. Instrum. and Meth. A305 (1991) 275.

[86] "The H1 Detector at HERA", I. Abt et al. (H1 Collaboration), DESY H1-96-01.

[87] A.C. Benvenuti et al., Nucl. Instrum. and Meth. A290 (1990) 353.

[88] R. Santonico and R. Cardorelli, Nucl. Instrum. and Meth. A187 (1981) 377;
R. Santonico and R. Cardorelli, Nucl. Instrum. and Meth. A263 (1988) 20.

[89] G. Cataldi et al. (E771 Collaboration), Nucl. Instrum. and Meth. A337 (1994) 350.

[90] I. Crotty et al. Nucl. Instrum. and Meth. A360 (1995) 512;
A. Ceron Zeballos et al. Nucl. Instrum. and Meth. A373 (1996) 35.

[91] C. Bacci et al. Nucl. Instrum. and Meth. A352 (1995) 350;
E. Cerron Zeballos et al. Nucl. Instrum. and Meth. A374 (1996) 132.

[92] Stan Majewski et al., Nucl. Instrum. and Meth. A348 (1994) 307.

[93] "The H1 Forward Muon Spectrometer", I.R. Kenyon et al., DESY 93-020 (1993).

[94] S. V. Golovkin et al., "Radiation damage studies on new liquid scintillators and liquid-core scintillating fibers", Nucl. Instrum. and Meth. A362 (1995) 283.

[95] E. Lorenz et al., "Fast readout of plastic and liquid scintillators by avalanche photodiodes", Nucl. Instrum. and Meth. A344 (1994) 64.

[96] R. De Salvo et al., "First results on the hybrid photodiode tube", Nucl. Instrum. and Meth. A315 (1992) 375.

[97] "ECFA/DESY Study of Physics and Detector for a Linear Collider", http://www.desy.de/conferences/ecfa-desy-lc96.html, proceedings to be published as DESY 97-123E.